

A STELLAR DYNAMICAL MASS MEASUREMENT OF THE BLACK HOLE IN NGC 3998 FROM KECK ADAPTIVE OPTICS OBSERVATIONS

JONELLE L. WALSH^{1,2}, REMCO C. E. VAN DEN BOSCH³, AARON J. BARTH², AND MARC SARZI⁴

¹Department of Astronomy, The University of Texas at Austin, 1 University Station C1400, Austin, TX 78712, USA; jlwalsh@astro.as.utexas.edu

²Department of Physics and Astronomy, University of California at Irvine, 4129 Frederick Reines Hall, Irvine, CA 92697, USA

³Max-Planck Institut für Astronomie, Königstuhl 17, D-69117 Heidelberg, Germany

⁴Centre for Astrophysics Research, University of Hertfordshire, AL10 9AB Hatfield, UK

Draft version May 7, 2012

ABSTRACT

We present a new stellar dynamical mass measurement of the black hole in the nearby, S0 galaxy NGC 3998. By combining laser guide star adaptive optics observations obtained with the OH-Suppressing Infrared Imaging Spectrograph on the Keck II telescope with long-slit spectroscopy from the *Hubble Space Telescope* and the Keck I telescope, we map out the stellar kinematics on both small spatial scales, well within the black hole sphere of influence, and on large scales. We find that the galaxy is rapidly rotating and exhibits a sharp central peak in the velocity dispersion. Using the kinematics and the stellar luminosity density derived from imaging observations, we construct three-integral, orbit-based, triaxial stellar dynamical models. We find the black hole has a mass of $M_{\text{BH}} = (8.1^{+2.0}_{-1.9}) \times 10^8 M_{\odot}$, with an *I*-band stellar mass-to-light ratio of $M/L = 5.0^{+0.3}_{-0.4} M_{\odot}/L_{\odot}$ (3σ uncertainties), and that the intrinsic shape of the galaxy is very round, but oblate. With the work presented here, NGC 3998 is now one of a very small number of galaxies for which both stellar and gas dynamical modeling have been used to measure the mass of the black hole. The stellar dynamical mass is nearly a factor of four larger than the previous gas dynamical black hole mass measurement. Given that this cross-check has so far only been attempted on a few galaxies with mixed results, carrying out similar studies in other objects is essential for quantifying the magnitude and distribution of the cosmic scatter in the black hole mass – host galaxy relations.

Subject headings: galaxies: active – galaxies: individual (NGC 3998) – galaxies: kinematics and dynamics – galaxies: nuclei

1. INTRODUCTION

Black holes reside at the centers of most massive galaxies (Magorrian et al. 1998; Richstone et al. 1998) and their masses (M_{BH}) are known to tightly correlate with properties of their host galaxy, like the bulge stellar velocity dispersion (σ_* ; e.g., Ferrarese & Merritt 2000; Gebhardt et al. 2000b; Tremaine et al. 2002; Gültekin et al. 2009b; Graham et al. 2011) and the bulge luminosity (L_{bul} ; e.g., Dressler 1989; Kormendy & Richstone 1995; Marconi & Hunt 2003; Gültekin et al. 2009b). Playing a fundamental role in establishing the empirical M_{BH} – host galaxy relationships over the past 15 years has been the *Hubble Space Telescope* (*HST*). In fact, *HST* spectroscopic observations have lead to about 50 of the 70 black hole mass measurements made to date.

More recently, adaptive optics (AO) systems on large ground-based telescopes have become an attractive alternative for obtaining high spatial resolution data. These systems correct for wavefront distortions caused by turbulence in the Earth’s atmosphere using a natural guide star or a laser guide star (LGS) as a reference. They are often used in conjunction with an integral field unit (IFU), which can map out the two-dimensional (2D) velocity field very efficiently compared to traditional long-slit spectrographs. In addition, AO systems operating in the near infrared on 8–10m telescopes are able to probe deep into the central regions of galaxies that previously presented significant observational challenges with the 2.4m *HST*, such as giant ellipticals with low-surface brightness cores and galaxy nuclei obscured by dust. AO-assisted IFUs will undoubtedly have a major impact on the field of supermassive black hole detection, and black hole mass mea-

surements using this technology have already become increasingly more prevalent in the literature (e.g., Houghton et al. 2006; Davies et al. 2006; Neumayer et al. 2007; Nowak et al. 2010; Rusli et al. 2011).

Measurements of black hole masses are most often made through the dynamical modeling of gas disks or stars. Gas dynamical modeling is conceptually simple, and the method can be applied to galaxies containing nuclear gas disks in circular rotation. The main drawback of this technique is that the gas can be influenced by non-gravitational forces, and the assumption of circular rotation must be verified. Furthermore, many of the observed gas disks in early-type galaxies exhibit velocity dispersions in excess of those expected from just rotational motion alone. This internal velocity dispersion can be quite large, ranging from ~ 100 – 500 km s^{-1} (e.g., van der Marel & van den Bosch 1998b; Verdoes Kleijn et al. 2002; Dalla Bontà et al. 2009). The physical nature of the intrinsic velocity dispersion is not understood. One interpretation is that the intrinsic velocity dispersion is the result of local microturbulence, but the bulk motion of the gas remains at the circular velocity (van der Marel & van den Bosch 1998b). Alternatively, the intrinsic velocity dispersion could be dynamically important, providing pressure support to the gas disk. Models that do not account for this effect will underestimate the true black hole mass (e.g., Barth et al. 2001; Neumayer et al. 2007; Walsh et al. 2010).

In contrast, stellar dynamical modeling is the most widely used method. However, extracting a secure black hole mass measurement from the observed kinematics can be challenging due to the complexity of the models. Recent adjustments to several previous stellar dynamical measurements

have been made after identifying significant systematic effects due to degeneracies between the dark matter halo and stellar mass-to-light ratio (Gebhardt & Thomas 2009), insufficient coverage of the phase space occupied by tangential orbits (Shen & Gebhardt 2010; Schulze & Gebhardt 2011), and the effects of triaxiality (van den Bosch & de Zeeuw 2010). Other possible sources of error, such as the choice of regularization (Valluri et al. 2004) and the uncertain inclinations of early-type galaxies (e.g., Verolme et al. 2002b; Gebhardt et al. 2003; Krajnović et al. 2005), have led to further debate about the accuracy of stellar dynamical mass measurements.

Since gas and stellar dynamical modeling methods suffer from different systematic effects, carrying out consistency tests between the two techniques is crucial. Only by applying both mass measurement methods to the same object can we address important unanswered questions regarding the black hole scaling relations. Is there a systematic difference between the masses derived from the two methods, and if so, how does this affect the slope of the relations? How much of the scatter in the M_{BH} – host galaxy relationships is the result of inconsistencies between stellar and gas dynamical measurements? Theoretical interpretations of M_{BH} – host galaxy correlations range from the black hole being an essential component in galaxy evolution (e.g., Silk & Rees 1998; Di Matteo et al. 2005) to simply being the result of random mergers without the need for a coevolution of black holes and galaxies (Peng 2007; Jahnke & Macciò 2011). Understanding the shape and cosmic scatter of the relations, especially at the sparsely populated upper- and lower-mass ends, are key to distinguishing between the various theories and for characterizing the black hole mass function.

This necessary consistency check has only been attempted on a few galaxies with mixed results. Stellar and gas dynamical models have been applied to IC 1459 (Verdoes Kleijn et al. 2000; Cappellari et al. 2002b) and NGC 3379 (Gebhardt et al. 2000a; Shapiro et al. 2006; van den Bosch & de Zeeuw 2010). Unfortunately, in both these galaxies, the gas kinematics turned out to be disturbed and not compatible with regular disklike rotation. Consequently, the ionized gas does not give a useful measurement of the black hole mass, and the galaxies are not suitable for a proper comparison between the two methods. In the cases of NGC 3227 and NGC 4151, the gas dynamical black hole mass measurements by Hicks & Malkan (2008) are generally consistent with the stellar dynamical masses reported by Davies et al. (2006) and Onken et al. (2007). However, Onken et al. (2007) could not find a single best fitting model for NGC 4151, and label their stellar dynamical result as tentative. Verdoes Kleijn et al. (2002) applied both methods to NGC 4335, and found a stellar dynamical mass that is at least five times larger than the gas dynamical determination. The black holes in M87 and Cen A have been the subject of numerous gas and stellar dynamical studies. While early examinations of the stellar dynamics (see review by Kormendy & Richstone 1995, and references therein) produced similar mass estimates for the black hole in M87 as the gas dynamical measurements (Harms et al. 1994; Macchetto et al. 1997), the most recent stellar dynamical mass from Gebhardt et al. (2011) is about a factor of two larger. Finally, there is a great variation in the Cen A gas dynamical black hole mass measurements, mainly due to uncertainties in the inclination of the gas disk (Marconi et al. 2001, 2006, Häring-Neumayer et al. 2006, Krajnović et al.

2007, Neumayer et al. 2007). The latest gas dynamical measurement of Neumayer et al. (2007) is significantly smaller than the stellar dynamical measurement of Silge et al. (2005) (by about a factor of four), but is in agreement with the stellar dynamical measurement by Cappellari et al. (2009). With only a few direct comparisons between the gas and stellar dynamical techniques, clearly more objects need to be examined.

An excellent target for such a comparison study is NGC 3998, which is a nearby, S0 galaxy with a low ionization nuclear emission-line region (LINER) nucleus (Ho et al. 1997). The galaxy has a simple morphology suitable for both stellar and gas dynamical modeling. The nuclear gas kinematics have been previously studied using multiple slit positions of the *HST* Space Telescope Imaging Spectrograph (STIS), and have been fit with a circularly rotating thin-disk model (de Francesco et al. 2006). With the de Francesco et al. (2006) measurement of $2.2 \times 10^8 M_{\odot}$ (scaled to our assumed distance), the black hole sphere of influence ($r_{\text{sphere}} = GM_{\text{BH}}/\sigma_{*}^2$) is expected to be $0''.15$, which can be resolved by IFUs combined with AO on 8–10m ground-based telescopes. NGC 3998 also contains a bright, compact nucleus that is suitable for use as a LGS tip-tilt reference. With the bulge stellar velocity dispersion reported by Gültekin et al. (2009b) of 305 km s^{-1} , this galaxy is further interesting as falls at the upper end of the $M_{\text{BH}} - \sigma_{*}$ relationship.

In this paper, we describe a measurement of the black hole in NGC 3998 using orbit-based stellar dynamical models. We will compare the stellar dynamical black hole mass measurement to the existing gas dynamical measurement by de Francesco et al. (2006) in order to test whether the two methods give consistent results when applied to the same galaxy. We begin by presenting the imaging observations and the determination of the galaxy’s stellar mass distribution in §2 and §3. We describe the spectroscopic observations in §4, and the measurement of the stellar kinematics in §5. Models of the point-spread function (PSF) are discussed in §6. In §7, we provide a brief overview of the stellar dynamical technique, and its application to NGC 3998, as well as present the modeling results in §8. Finally, in §9, we examine the stellar orbital structure of the galaxy, compare the stellar dynamical mass measurement to gas dynamical determination, and place the black hole in NGC 3998 on the M_{BH} – host galaxy relationships. Throughout this paper, we adopt a distance to NGC 3998 of 13.7 Mpc (Tonry et al. 2001; Mei et al. 2007).

2. IMAGING OBSERVATIONS

Imaging observations are essential components in the orbit-based stellar dynamical models, and are used to derive the galaxy’s luminosity density. We obtained a Wide Field Planetary Camera 2 (WFPC2) F791W image of NGC 3998 centered on the Planetary Camera (PC) detector from the *HST* archive. The *HST* image of NGC 3998 was originally acquired under program GO-5924, and the total exposure time was 100 s. The WFPC2 image, with a pixel scale of $0''.046$ and $0''.1$ for the PC and Wide-Field chips, provides high angular resolution imaging suitable for constructing a luminous mass model near the black hole, however the image only extends out to a radius of $\sim 10''$ (0.6 kpc). We therefore also included in the analysis a deep *Ks*-band image (courtesy of Läsker et al., in preparation) taken with the Wide-field InfraRed Camera (WIRCam; Puget et al. 2004) on the 3.6m Canada-France-Hawaii Telescope (CFHT). The image has a

spatial scale of $0''.3 \text{ pixel}^{-1}$ and covers a $30' \times 30'$ field. The total exposure time was 442 s, and we were able to measure the galaxy’s surface brightness profile out to a radius of $\sim 250''$ (16.6 kpc). The ground-based image was used to generate the mass model on large spatial scales, which is helpful in constraining the intrinsic shape of the galaxy in the stellar dynamical models.

3. STELLAR MASS PROFILE

We parameterized the WFC2 F791W and WIRCam K_s -band images of NGC 3998 as the sum of 2D Gaussians using the Multi-Gaussian Expansion (MGE) method (Cappellari 2002a). The MGE method has often been used to model high-resolution and ground-based images (e.g., Verolme et al. 2002b; Cappellari et al. 2006; Onken et al. 2007; Dalla Bontà et al. 2009; Krajnović et al. 2009), and we used the MGE method here because it has the advantage of being able to reproduce a large range of density distributions while also allowing for the deprojection to be carried out analytically. MGE models were fit to both images simultaneously while also accounting for the *HST* PSF. The PSF itself was described as the sum of 25 positive and negative Gaussians, which were found by applying the MGE software to a Tiny Tim model (Krist & Hook 2004). Our best-fit MGE parametrization of the galaxy was composed of 12 Gaussians, where the innermost Gaussian was constrained to be round and the position angles (PA) of the Gaussian components were required to be the same. This model produced an excellent fit to the imaging data, as can be seen in Figure 1. In addition, in Figure 2, we present the surface brightness profile, the MGE model, and the percent error averaged along the azimuthal axis. The MGE model was corrected for galactic extinction using the Schlegel et al. (1998) values given by the NASA/IPAC Extragalactic Database and the surface density was converted to I -band solar units using the WFC2 calibration by Dolphin (2000). In Table 1, we provide the best-fit values of the MGE parameters. We further note that there are no significant emission lines within the F791W bandpass (Ho et al. 1993).

Although our adopted MGE model requires each Gaussian component to have the same PA, we fit an additional MGE model that allowed for isophotal twists. We detected very small changes to the PA, of typically $< 1^\circ$, between the components. Furthermore, when using this MGE parameterization as input into the orbit-based stellar dynamical models, we found worse agreement between the observed and predicted stellar kinematics. As a result, we do not consider the MGE model that allows for isophotal twists any longer, and focus solely on the MGE parameterization that constrains each component to have the same PA.

When constructing mass models of galaxies containing an active galactic nucleus (AGN), often the innermost Gaussian of the MGE model is assumed to arise from non-thermal emission and is excluded from the stellar mass distribution. The nucleus of NGC 3998 has been spectroscopically classified as a Type 1.9 LINER (Ho et al. 1997), and an unresolved, variable UV source, a compact radio source, and an X-ray source have all been detected at the galaxy’s center (Hummel et al. 1984; Fabbiano et al. 1994; Maoz et al. 2005; Roberts & Warwick 2000; Pellegrini et al. 2000). All of this evidence suggests that NGC 3998 hosts an AGN. However, the galaxy also exhibits a cuspy surface brightness profile, and some starlight may still be contained within the innermost Gaussian. We therefore ran orbit-based stellar dynamical

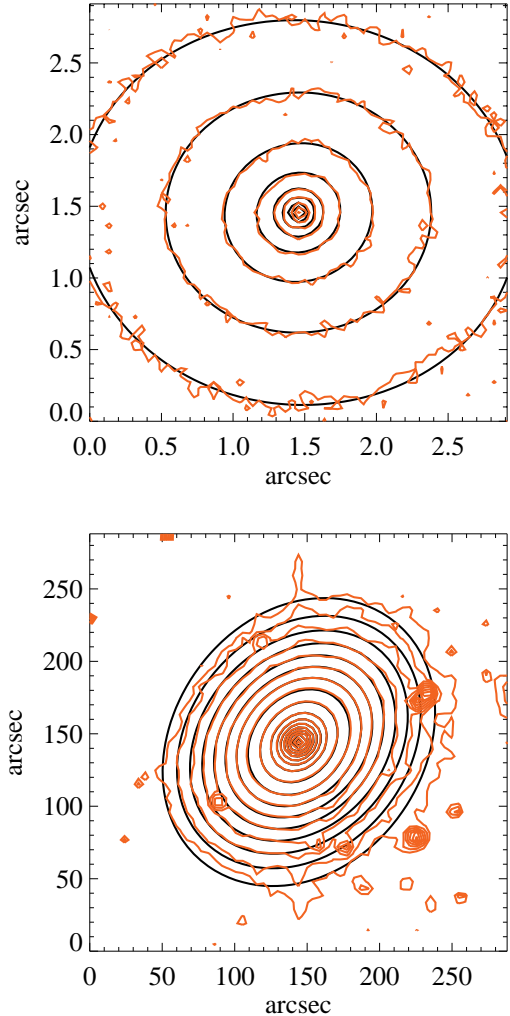


FIG. 1.— Isophotes of the MGE model (black) are compared to the inner regions of the *HST* WFC2/PC F791W image (top) and the CFHT WIRCam K_s -band image (bottom) of NGC 3998. Contours are logarithmically spaced, but arbitrary.

cal models using MGE parameterizations that both included and excluded this central Gaussian, and will discuss the results in §8 and §8.1. These descriptions represent the two extremes: in one case all the light from the innermost Gaussian is attributed to the stars and in the other scenario all the light is assigned to the AGN.

4. SPECTROSCOPIC OBSERVATIONS

We observed NGC 3998 using the IFU OH-Suppressing Infrared Imaging Spectrograph (OSIRIS; Larkin et al. 2006) assisted by the LGS AO system (Wizinowich et al. 2006; van Dam et al. 2006) on the 10-m Keck II telescope. The OSIRIS data provided high angular resolution observations of the stellar kinematics over a 2D field and allowed us to resolve r_{sphere} . We also retrieved archival STIS observations of NGC 3998 from the *HST* archive. The STIS observations have a well-characterized PSF and provided us with additional high-resolution data of the stellar kinematics along a single PA. Preliminary work from a stellar dynamical analysis using this same STIS data was described by Bower et al. (2000). Past studies have shown the importance of acquiring large-

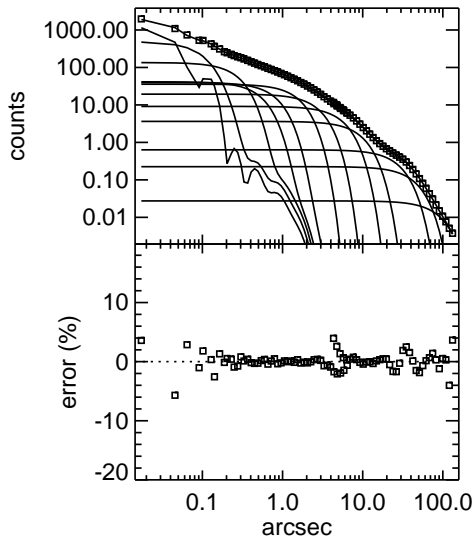


FIG. 2.— *Top panel:* Comparison between the observed surface brightness profile (open squares) and the best-fitting MGE model (solid line) averaged along the azimuthal axis. Individual components making up the MGE model, which have been convolved with the *HST* PSF, are also shown. *Bottom panel:* The percent error between the model and data.

TABLE 1
BEST-FIT MGE PARAMETERS

j (1)	$\log I_j$ ($L_{\odot,1} \text{ pc}^{-2}$) (2)	σ'_j ($''$) (3)	q'_j (4)
1	6.445	0.017	0.990
2	5.405	0.078	0.940
3	4.808	0.223	0.962
4	4.445	0.504	0.946
5	3.814	1.037	0.756
6	4.096	1.200	0.903
7	3.973	2.042	0.881
8	3.641	4.134	0.799
9	3.347	7.223	0.813
10	2.444	21.210	0.796
11	2.149	34.812	0.776
12	1.034	73.492	0.866

NOTE. — Column (1) gives the Gaussian component number, column (2) is central surface brightness of each Gaussian, column (3) provides the dispersion of Gaussian along the major axis, and column (4) lists the axis ratio. All of the Gaussian components were constrained to have the same position angle, which was determined to be -41.5° . The primed variables indicate projected quantities. Stellar dynamical models were run using MGE models that both include and exclude the central component ($j = 1$).

scale observations of the kinematics in order to properly constrain the orbital distribution in the stellar dynamical models (e.g., Shapiro et al. 2006; Krajnović et al. 2009). For this reason, we also obtained long-slit observations using the Low-Resolution Imaging Spectrograph (LRIS; Oke et al. 1995) on the 10-m Keck I telescope. In the sections that follow we describe the OSIRIS, STIS, and LRIS observations and data reduction.

4.1. LGS AO OSIRIS Observations

The OSIRIS observations were acquired on 2009 May 1 and 2 during the first half of each night. We used the $0''.05$ spatial scale and the broadband *K* (*Kbb*) filter, providing coverage of $1.965\text{--}2.381 \mu\text{m}$. We aligned the long axis of the IFU with the major axis of the nuclear emission-line disk at $\text{PA} = 308^\circ$ (de Francesco et al. 2006). Using the nucleus of NGC 3998 as the tip-tilt reference, we were able to achieve a good AO correction and we estimate that the PSF core had a full width at maximum intensity (FWHM) of $\sim 0''.1$ (see §6). We obtained 300 s exposures of the galaxy nucleus and sky, following the sequence Object-Object-Object-Sky Object-Object-Object-Sky, and recorded 3.8 hours of on-source integration time. Each object exposure was dithered $0''.2$ perpendicular to the long-axis of the IFU in order to remove bad pixels and to obtain a slightly wider field of view of $1''.2 \times 3''.2$. In addition, we observed K and M giant stars for use as velocity templates in the same observational setup as was used for the galaxy, and A0 V stars for telluric correction.

The data were reduced using the OSIRIS data reduction pipeline v2.3⁵. The pipeline includes subtraction of a sky frame, glitch identification and cosmic ray cleaning, extraction of the spectra into a data cube (with two spatial dimensions, x and y corresponding to the short and long axis of the IFU, and one spectral dimension), wavelength calibration, atmospheric dispersion correction, and telluric correction using the extracted one-dimensional (1D) spectrum of an A0 V star. While the reduction pipeline is capable of performing scaled sky subtraction following the algorithm outlined by Davies (2007), we found that the current implementation did not work well for our data set and produced strong sky residuals in the reduced cubes. We instead opted for a direct subtraction method, where we subtracted a sky exposure from the previous two object frames and from the following object frame. Thus, the sky and object frames were separated in time by at most 600 s, and the direct subtraction method worked well. After all of the individual galaxy cubes were reduced, we determined the spatial x and y offsets between the first galaxy cube and each of the remaining object cubes. This was done by summing along the wavelength axis of the data cubes to generate flux maps, then cross-correlating the images. Using these offsets, the individual object cubes were aligned and averaged to produce the final galaxy data cube. The velocity template star observations were reduced in a similar manner, but an additional step was included to extract a 1D spectrum from the data cube using a circular aperture with a radius of 7 pixels.

4.2. Archival STIS Observations

We retrieved STIS observations of NGC 3998 made on 1999 March 10 under program GO-7350 from the *HST* archive. NGC 3998 was observed with the 52×0.2 aperture at eight slit positions, all of which were aligned at a PA of 152° , within 15° of the galaxy's major axis. Two successive exposures were obtained at each slit position to aid in the removal of cosmic rays, and a shift of about four pixels in the spatial direction was made between positions. The average exposure time recorded at each slit position was 2730 s. The G750M grating, centered on 8561 \AA , was read out in an unbinned mode, which provided a scale of $0''.0507 \text{ pixel}^{-1}$ along

⁵ <http://irlab.astro.ucla.edu/osiris/pipeline.html>

the spatial axis and $0''.554 \text{ \AA pixel}^{-1}$ along the dispersion direction. Following the observation of the galaxy at each slit position, a contemporaneous flat field was taken.

In addition to the galaxy observations, the K3 III star HR 260 was observed as part of Program 7350 for use as a velocity template. In order to build up a larger library, we also searched the *HST* archives for other suitable stars, using as a guide the previously published stellar dynamical black hole mass measurements made from STIS data. We retrieved an additional four stars, observed using the same STIS setup, from the archive: the K0 III star HR 7615 (GO-7566), the G8 III star HD 141680 (GO-8591), and the K2 III and G5 V stars HD 73471 and HD 115617 (GO-8928).

The data were reduced by running individual IRAF⁶ tasks within the standard Space Telescope Science Institute (STScI) CALSTIS pipeline. With these tasks, the overscan region was trimmed, the bias and dark files were subtracted, flat-field corrections were applied, CR-split exposures were combined to reject cosmic rays, wavelength and flux calibration were performed, and the data were rectified for geometric distortions. We chose to run individual segments of the pipeline independently, following the procedure detailed in the STIS Data Handbook v6.0 (Bostroem & Proffitt 2011), instead of running the wrapper CALSTIS program so that a couple of important modifications could be made.

Specifically, we found that the dark calibration file provided by STScI, which is constructed from several long dark exposures taken over the course of a week, contained very strong hot pixels that did not subtract well and left numerous negative pixels in the galaxy spectral images. This poor subtraction is likely due to pixels that vary on timescales of less than a week. We therefore followed a similar approach to Bower et al. (2001), and modified the dark file by replacing any pixels that deviated by more than 8σ with a median value. After the initial processing was complete, we included an additional cleaning step and used LA-COSMIC (van Dokkum 2001) to remove the hot pixels remaining after the subtraction our modified dark file. We then applied the geometric distortion correction to the cleaned images. Additionally, we used the contemporaneous flat field exposures taken at each of the slit positions to remove the obvious fringe pattern affecting the spectra. IRAF tasks were used to reduce and normalize the flat field observations, shift and scale the fringes in the normalized flat such that they would match those in the galaxy images, and to finally apply the fringe correction.

The reduced, geometrically rectified, fringe-corrected spectral images at each of the eight slit positions taken along the galaxy's major axis were then aligned and combined to produce the final 2D galaxy spectrum. The same procedure was applied to the five velocity standard stars observed with STIS, but as a final step, we constructed a 1D spectrum by adding together 3 spectral rows above and below the central row from the 2D images.

4.3. Long-Slit LRIS Observations

The LRIS observations were obtained during the first half night on 2009 April 15. On the red side, we used the 831 lines mm^{-1} grating centered on 8200 \AA with a $1''$ -wide slit, producing a scale of $0.92 \text{ \AA pixel}^{-1}$ in the dispersion direction and $0''.211 \text{ pixel}^{-1}$ in the spatial direction. We placed the long-slit

along four PAs: along the major axis of the nuclear gas disk (PA = 308° ; de Francesco et al. 2006), along the minor axis (PA = 218°), and at two intermediate angles (PA = 353° and PA = 263°). At each PA we acquired a $2 \times 600 \text{ s}$ observation, with the exception of the minor axis PA, where we recorded a $2 \times 300 \text{ s}$ observation. Between individual exposures, we dithered by $90''$ along the length of the slit. We additionally observed K giant stars for use as velocity templates, and the flux standard star Feige 34, in the same observational setup as was employed for NGC 3998.

We reduced the LRIS data using IRAF. The initial processing steps of the 2D spectral images included trim and bias subtraction, flat fielding, and cosmic ray cleaning. For the NGC 3998 exposures, we also geometrically rectified the 2D spectra so that both the wavelength and spatial axes would run parallel along rows and columns, respectively. During this process, we used the Hg, Ar, and Ne arc lamp exposures acquired immediately following the NGC 3998 observations to wavelength calibrate the spectral images. We removed the sky background by subtracting the two dithered spectral images taken at each PA from one another. The difference images were spatially aligned, averaged together, and trimmed to remove the negative features resulting from the pair subtraction. As a final reduction step, we compared a calibrated 1D standard star spectrum to a 1D spectrum of the galaxy extracted using the APALL task to determine the multiplicative factor (as a function of wavelength) that was needed to bring the two spectra into agreement. The scaling was then applied to the 2D galaxy spectrum to produce a final, flux-calibrated spectral image of NGC 3998 at each PA.

The velocity template stars were reduced following a slightly different procedure because we only required a 1D spectrum from the 2D image. After the initial image processing, we applied the same spectral rectification and wavelength calibration to the 2D spectra of the velocity template stars as was used for the NGC 3998 spectra. We performed a secondary correction to the wavelength calibration by applying a small linear shift along the dispersion axis so that two bright sky lines bounding the Ca II triplet region matched the known wavelengths of 8430 \AA and 8886 \AA . We then extracted a 1D spectrum with APALL using a $5''.3$ aperture radius and sky regions that were $8''.4$ in width beginning at a distance of $23''$. The velocity template spectra were flux calibrated using an extracted 1D spectrum of the standard star Feige 34.

5. MEASURING THE STELLAR KINEMATICS

From the OSIRIS, STIS, and LRIS data, we extracted 1D spectra over a range of spatial locations and measured the line-of-sight velocity distribution (LOSVD), which we parameterized with the first four Gauss-Hermite moments (V , σ , h_3 , and h_4). Measurement of the LOSVD requires spectra with a high signal-to-noise ratio (S/N). Typically, a S/N of ~ 40 per spectral and spatial resolution element are needed in order to reliably determine h_3 and h_4 , which quantify asymmetric and symmetric deviations from a Gaussian (e.g., van der Marel & Franx 1993; Bender et al. 1994; Statler 1995; Krajnović et al. 2009). We used the Voronoi binning algorithm (Cappellari & Copin 2003) in order to achieve the best spatial resolution possible given such a requirement on the minimum S/N. The stellar kinematics in each of the spatial bins were then measured using the penalized pixel fitting (pPXF) method of Cappellari & Emsellem (2004). With this method, logarithmically rebinned galaxy spectra are fit in pixel space using a stellar template that is

⁶ IRAF is distributed by the National Optical Astronomy Observatory, which is operated by the Association of Universities for Research in Astronomy under cooperative agreement with the National Science Foundation

convolved with the LOSVD.

The pPXF code minimizes template mismatch by finding an optimal stellar template that is composed of a linear combination of spectra from a library. The libraries were designed to contain stars that are representative of the galaxy’s expected stellar population. When measuring the stellar kinematics from the OSIRIS data, we used a template library composed of 20 stars, consisting of mostly K and M giants (spectral types K0 – K5 and M0 – M5), a K4 V star, and a G9 V star. The STIS kinematics were determined using a library of five stars (G8 III – K3 III, and G5 V), and the LRIS kinematics were extracted using a library of eight K0 III – K3 III stars.

The optimal stellar template was determined just once by using pPXF to fit a very high S/N spectrum generated by summing the spectra over all spatial locations. Once the optimal stellar template was found, pPXF was used to measure the kinematics in each spatial bin by holding fixed the relative weights of the stars that comprise the optimal template. We did, however, allow the coefficients of an additive Legendre polynomial of degree 1 and a multiplicative Legendre polynomial of degree 2 to vary. The additive polynomial was used to model the AGN continuum, and the multiplicative polynomial was included to correct continuum shape differences between the optimal stellar template and the galaxy spectra due to imperfect flux calibration and reddening.

Errors on the kinematic measurements were estimated using a set of Monte Carlo simulations. During each realization, random Gaussian noise was added to the observed spectrum from each bin based upon the standard deviation of the pPXF model residuals. The LOSVD was measured with the penalization turned off in order to produce realistic uncertainties. From 100 realizations, we determined the 1σ errors from the standard deviation of the resulting distributions.

We also tested the robustness of our kinematic measurements by assuming different continuum models, each with various combinations of additive and multiplicative polynomials of degree 1–3. We additionally used pPXF to measure just V and σ in each spatial bin, as well as allowed for the relative contributions of the stars making up the optimal stellar template to vary between spatial bins. Regardless of the continuum model used, the number of Gauss-Hermite moments extracted, or whether a new optimal template was fit for each bin, we found consistent results for all but a few spatial bins. The kinematics measured from these few spatial bins were deemed unreliable and excluded from further analysis.

As a final step, we determined the systematic offsets in the odd Gauss-Hermite moments directly from the data using the point-symmetrization routine described in Appendix A of van den Bosch & de Zeeuw (2010). The offset for the first odd Gauss-Hermite moment corresponds to the recession velocity of the galaxy, and a systematic shift in the second odd Gauss-Hermite moment may result from slight template mismatch effects. The offsets were subtracted from the V and h_3 values determined with pPXF.

Although the systematic offsets in the odd moments were measured with the point-symmetrization code, we did not symmetrize the kinematics before using them as inputs into the orbit-based dynamical models. Often the observed kinematics are symmetrized (e.g., Gebhardt et al. 2003; Cappellari et al. 2006) because the dynamical models can only produce predicted kinematics that are bi- or point-symmetric. Thus, symmetrizing the input kinematics reduces the noise in the observations and aids in visual comparisons between various models. However, the symmetrization rou-

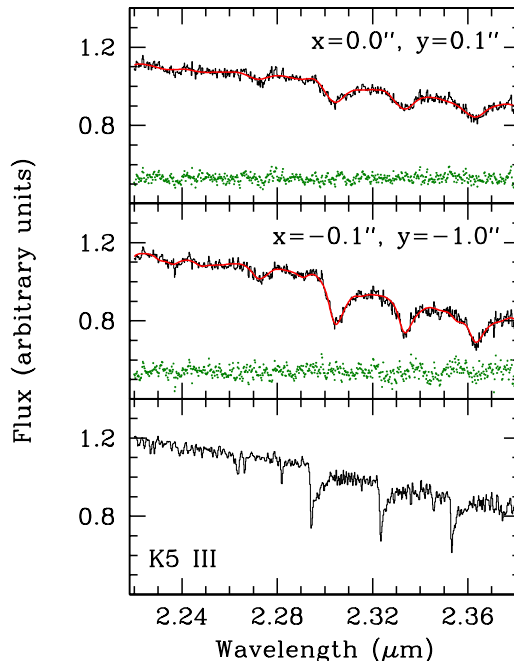


FIG. 3.— The best-fit broadened optimal stellar template (red) is compared to the observed NGC 3998 spectrum from a single OSIRIS lenslet located at $x=0.0''$, $y=0.1''$ (top) and a spatial bin containing 25 OSIRIS lenslets centered on $x=-0.1''$, $y=-1.0''$ (middle). Green dots show the fit residuals and have been shifted by an arbitrary amount. The optimal template used to measure the kinematics is dominated by a K5 III star, whose spectrum is shown in the bottom panel.

tine assumes that the galaxy nucleus is exactly centered on one of the IFU lenslets. While this is true for the reduced data sets from the SAURON IFU (Bacon et al. 2001), for which the symmetrization code was originally designed, the assumption does not hold for the OSIRIS data. Consequently, our best-fit stellar dynamical model, presented in §8, was determined using non-symmetrized kinematics, but in §8.1 we also test the effect on M_{BH} of symmetrizing the kinematics before running the orbit-based stellar dynamical models.

5.1. OSIRIS Kinematics

We used the pPXF method to measure the kinematics from the OSIRIS data over a wavelength range of 2.22–2.38 μm . For NGC 3998, this wavelength region included three very strong CO bandhead absorption features: $(2-0)^{12}\text{CO}$, $(2-1)^{12}\text{CO}$, and $(4-2)^{12}\text{CO}$. The kinematics were constrained mainly by these prominent CO bandheads, although weaker Ca I and Mg I absorption lines were also detected. We note that no emission lines were detected with the OSIRIS Kbb filter. The stellar kinematics were measured from 90 spatial bins, 10 of which contain just a single lenslet and fall within the central $\sim 0.15''$ region. The S/N of the spectra (taken to be the ratio of median value of the binned spectrum to the standard deviation of the pPXF model residuals) ranged from 39–73, with a median value of 58. The optimal template was composed of eight stars, with a K5 III star contributing a majority of the flux. In Figure 3, we show example spectra from two spatial bins and the optimal template broadened by the best-fit LOSVD, as well as the spectrum from the K5 III star.

The kinematics show that the galaxy is rapidly rotating,

with velocities of $\pm 115 \text{ km s}^{-1}$ over the OSIRIS IFU, and there is an anti-correlation between h_3 and V . Although the h_4 kinematics are expected to be symmetric about the center, with a peak or dip at the nucleus, we find h_4 to be noisy, without any clear trends. In contrast, the velocity dispersion shows a very strong peak at the nucleus, rising from $\sigma \sim 270 \text{ km s}^{-1}$ in the outer regions to $\sigma \sim 560 \text{ km s}^{-1}$ at the center. The errors on the velocity dispersion measurements are quite large at nucleus and will be discussed further in §8.1, but outside of the innermost lenslets, we find typical errors of 10 km s^{-1} , 13 km s^{-1} , 0.02 , and 0.03 , for V , σ , h_3 , and h_4 , respectively.

NGC 3998 contains an AGN, which dilutes the observed stellar features, and can lead to difficulties in extracting the kinematics near the nucleus. During the spectral fitting with pPXF, we included an additive polynomial to account for the AGN dilution. However, we measured large uncertainties on the kinematics extracted from four of the innermost lenslets, suggesting that pPXF cannot disentangle the AGN from the stellar component in a consistent manner. Our final best-fit model presented in §8 was found using the kinematic measurements and errors from all the OSIRIS bins, however we further tested the effect on M_{BH} when the central kinematics are excluded from the modeling (see §8.1).

5.2. STIS Kinematics

We measured the stellar kinematics from the Ca II triplet lines using the pPXF routine to fit an optimal stellar template over the wavelength range $8420\text{--}8830 \text{ \AA}$. The optimal template was composed of two stars: a K2 III star, which contributed most of the flux to the template, and a K3 III star. Near the nucleus, there was substantial AGN contamination, which diluted the Ca II triplet lines, as well as a clear detection of an emission line, which is most likely the [Fe II] line at a rest wavelength of 8618 \AA . During the spectral fitting, we excluded a 50 \AA wavelength region surrounding this emission feature to prevent biases when measuring the LOSVD. Furthermore, we were unable to measure the stellar kinematics within $\sim 0''.2$ of the nucleus due to the AGN. In the end, we extracted reliable kinematics from eight spatial bins extending from about $0''.2$ to $1''$ from the nucleus. The spectra in the eight bins had a S/N of $31\text{--}40$ with a median value of 38 . We present the nuclear spectrum of NGC 3998, along with examples of the spectral fitting for two bins from which the stellar kinematics could be measured in Figure 4.

Like the OSIRIS kinematics, the STIS kinematics show that the galaxy is rotating quickly with velocities of $\pm 100 \text{ km s}^{-1}$ over the inner $\pm 1''$, that there is a rise in velocity dispersion from $\sigma \sim 290 \text{ km s}^{-1}$ at $1''$ to $\sigma \sim 370 \text{ km s}^{-1}$ at $0''.2$, and that h_3 is anti-correlated with the velocity. Again, we are unable to detect any significant trends in h_4 . The median errors on the STIS kinematics were 21 km s^{-1} , 25 km s^{-1} , 0.05 , and 0.06 for V , σ , h_3 , and h_4 , and are larger than the uncertainties on the OSIRIS kinematics due to lower S/N spectra. Given these uncertainties, the STIS data should not have a substantial impact on the M_{BH} determination, and we found that this was indeed the case when running tests that excluded the STIS measurements. However, for completeness, the final best-fit model described in §8 was determined using the STIS data, along with the OSIRIS and LRIS measurements.

5.3. LRIS Kinematics

We used the pPXF method to measure the kinematics from the Ca II triplet lines over a wavelength range of $8480 \text{ \AA} -$

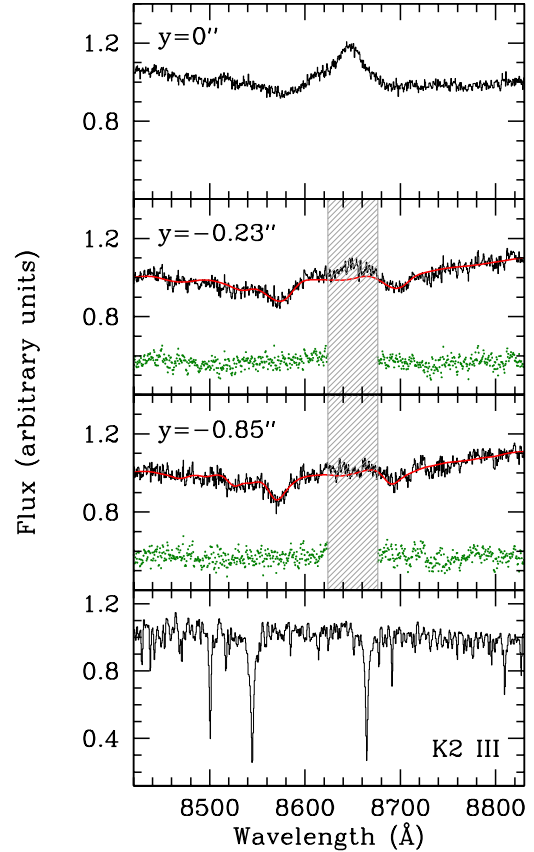


FIG. 4.— STIS spectra extracted from bins located $0''.0$, $-0''.23$, and $-0''.85$ from the nucleus are shown in the top three panels. As can be seen in the top panel, the AGN prevents the galaxy’s stellar kinematics from being measured near the nucleus, and the [Fe II] emission line is clearly detected. Beyond $\sim 0''.2$ from the nucleus, we were able to measure the stellar kinematics, and the middle two panels provide examples of the spectral fitting. The best-fit broadened optimal template is plotted in red, and the fit residuals are shown by the green dots, which have been shifted upward by an arbitrary amount. The grey shaded box denotes the wavelength region that was excluded during the spectral fitting. The bottom panel shows the STIS spectrum of a K2 III star, which contributed most of the flux to the optimal stellar template.

8830 \AA . The kinematics in each spatial bin were determined using an optimal stellar template constructed from the linear combination of a K3 III and a K0 III star. Ultimately, the kinematics were measured from a total of 170 spatial bins over the four PAs. The S/N in the bins ranged from $60\text{--}107$, with a median value of 82 . We present example fits to the galaxy spectra in addition to the K3 III template in Figure 5.

We were able to measure the kinematics out to $\sim 15''$ ($\sim 1 \text{ kpc}$) along the major axis and along the intermediate angles of $\text{PA} = 353^\circ$ and $\text{PA} = 263^\circ$. The kinematics along the minor axis were measured out to $\sim 8''$. The large-scale kinematics exhibit features similar to those seen from the high-resolution OSIRIS maps and STIS data. The stars show rotation with V between $\pm 200 \text{ km s}^{-1}$, the velocity dispersion increases steeply toward the center to values of $350\text{--}400 \text{ km s}^{-1}$, and h_3 is anti-correlated with V across the inner $\sim 10''$. In addition, we find that h_4 is symmetric about the center with a slight peak to values of 0.05 at the nucleus. The median errors for V , σ , h_3 , and h_4 were 8 km s^{-1} , 9 km s^{-1} , 0.02 , and 0.03 for V , σ , h_3 , and h_4 .

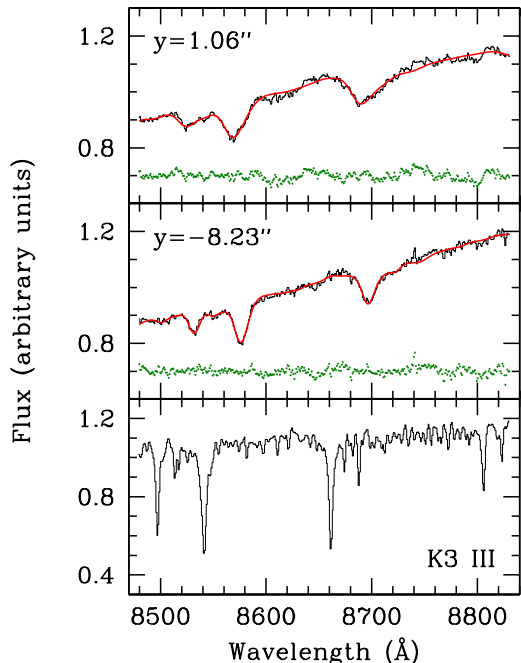


FIG. 5.— Examples of the spectral fitting to the LRIS data. The spectra were extracted from bins located $1''.06$ (top) and $-8''.23$ (middle) from the nucleus. The optimal stellar template, broadened by the best-fit LOSVD, is shown in red, and the fit residuals are displayed in green. For comparison, we plot the LRIS spectrum of the K3 III star that contributes most of the flux to the optimal stellar template.

We find excellent agreement between kinematics measured from the OSIRIS, STIS, and LRIS data. While template mismatch is a common source of uncertainty when extracting stellar kinematics, at least it is encouraging to find consistent measurements from different instruments over different wavelength regions using different velocity template stars. In Figure 6, we show the four Gauss-Hermite moments measured from the three different instruments as a function of projected distance from the nucleus.

6. PSF MEASUREMENTS

An important input into the stellar dynamical models is the spatial PSF. However, determining the OSIRIS PSF is especially complicated because the quality of the AO correction varies with time and numerous data cubes (obtained over the course of two nights) were mosaiced together. Davies et al. (2004) highlight several ways to estimate the PSF from AO-corrected IFU data, and for this work we used a method that compares the OSIRIS data cube to a deconvolved *HST* image, as has been employed by Krajnović et al. (2009). We used the MGE model generated from the WFPC2 791W image (discussed in §3), which already has the *HST* PSF removed, and convolved it with a model for the OSIRIS PSF. The OSIRIS PSF is taken to be three concentric circular 2D Gaussians parameterized by the dispersions and relative weights of the components. The convolved image is then compared to the OSIRIS data cube, summed along the wavelength axis, and the parameters of the PSF are varied to determine the best fit. We found that the three components have dispersions of $0''.01$, $0''.04$, and $0''.28$ with relative weights of 0.19, 0.60, and 0.21. Thus, we were able to achieve a good AO correction and the

PSF core has a FWHM of $\sim 0''.1$.

To model the STIS PSF, we used Tiny Tim (Krist & Hook 2004) to reconstruct the PSF for a monochromatic filter pass-band at 8651 \AA . Fitting two concentric circular 2D Gaussians to the Tiny Tim image, we found that the PSF can be characterized by a narrow component with $\sigma = 0''.03$ and a weight of 0.76, plus a broad component with $\sigma = 0''.12$ and a weight of 0.24. These dispersion values and weights were used as input into the stellar dynamical models, which require a PSF to be described with circularly symmetric Gaussians.

For the LRIS PSF, we examined the spatial distribution of the eight velocity template stars that were observed on the same night as NGC 3998. We fit a single Gaussian to a spatial cut at 8600 \AA through the geometrically rectified 2D spectra, and found an average dispersion of $\sigma = 0''.35$.

7. ORBIT-BASED STELLAR DYNAMICAL MODELING

Orbit-based dynamical models using the Schwarzschild superposition method (Schwarzschild 1979) are the standard means by which to measure black hole masses from stellar kinematics (e.g., Gebhardt et al. 2003; Valluri et al. 2005; Gültekin et al. 2009a; Cappellari et al. 2009). They are additionally useful for studying the orbital structure of galaxies (e.g., Verolme et al. 2002b; Krajnović et al. 2005; Cappellari et al. 2006; Shen & Gebhardt 2010), and constraining dark matter halo properties (e.g., Thomas et al. 2005, 2007, Weijmans et al. 2009; Forestell & Gebhardt 2010; Murphy et al. 2011). The main strength of this technique is that a self-consistent distribution function can be constructed from the observables, without the need for assumptions about the orbital anisotropy. Here, we calculate three-integral, triaxial, Schwarzschild models using the implementation of van den Bosch et al. (2008), which was based upon the previous work of Rix et al. (1997), van der Marel et al. (1998a), Cretton et al. (1999), Verolme & de Zeeuw (2002a), and Cappellari et al. (2006). We provide a brief summary of the method here, but refer the reader to van den Bosch et al. (2008) for a comprehensive description of model.

In the model, the galaxy potential consists of contributions from the black hole, the stars, and dark matter. We take the three-dimensional (3D) stellar mass to be described as the sum of multiple coaxial Gaussian distributions, which are determined by deprojecting the MGE model and assuming a constant stellar mass-to-light ratio (M/L). The deprojection is carried out by choosing a direction from which the galaxy is observed, characterized by the Euler angles θ (corresponding to the inclination angle), ϕ , and ψ . With a set of these viewing angles, each component j of the MGE model is uniquely deprojected into a 3D Gaussian with a shape given by p_j , q_j , and u_j , which are the ratios between the intermediate and long axes, the short and long axes, and the length of the longest axis of the projected Gaussian on the sky to the long axis, respectively. For details about the deprojection and the relations between the viewing angles and intrinsic shape parameters see van den Bosch et al. (2008). The Schwarzschild method additionally allows for dark halo properties to be determined, but our stellar kinematics extend out to a radius of $\sim 15''$ (~ 1 kpc), and we are unable to differentiate between various dark halo models. Consequently, the model results presented in §8 do not include dark matter, and the galaxy potential is calculated from the contributions of the black hole and the stars alone. However, we do test the effect on the inferred black hole mass by incorporating a couple of fixed dark halo models in §8.1.

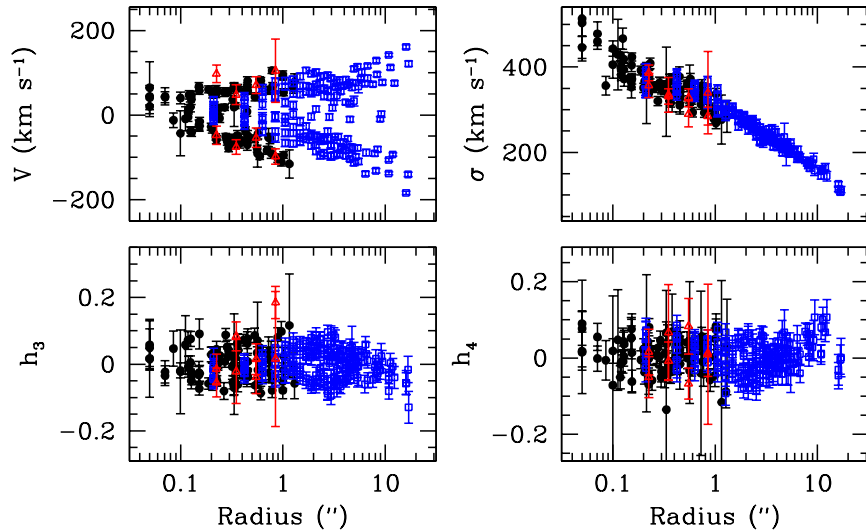


FIG. 6.— A comparison of the stellar kinematics for NGC 3998 measured from the OSIRIS (black circles), STIS (red triangles), and LRIS (blue squares) data. The radial velocity, V , the velocity dispersion, σ , and the higher-order Gauss-Hermite moments, h_3 and h_4 , which quantify asymmetric and symmetric deviations from a Gaussian, are plotted as a function of projected distance from the nucleus. There are two velocity branches in the top left plot due to the galaxy’s rotation: one side of the galaxy is blueshifted relative to the systemic velocity and the other side is redshifted. The high angular resolution kinematics from both OSIRIS and STIS are in agreement with the large-scale data from LRIS.

Given the galaxy potential, a representative orbit library is generated, and the initial conditions of the orbits are chosen such that the three integrals of motion are sampled. The orbits are integrated and projected onto the observable quantities (the location on the sky and the LOSVD parameters) while accounting for the PSF and aperture binning. Next, weights for each orbit are found such that superposition of orbits matches the kinematics in the least-squares sense while also satisfying constraints imposed by the stellar density in each aperture and 3D bin. Many dynamical models are calculated with different values for the parameters of interest, namely M_{BH} , M/L , and the viewing angles θ , ϕ , and ψ (or equivalently the intrinsic shape parameters p , q , and u). Finally, the best model is taken to be the one that most closely matches the data in the χ^2 sense.

We fit the Schwarzschild models to the OSIRIS, STIS, and LRIS kinematics presented in §5 and use the stellar density distribution constructed from the MGE models both with and without the innermost Gaussian component discussed in §3. The MGE model that includes the central Gaussian component will be discussed in §8, and the model that assigns all the light from the innermost component to the AGN will be described in §8.1. With four Gauss-Hermite moments measured in each of the 90 OSIRIS bins, 8 STIS bins, and 170 LRIS bins, there are 1072 observables. The orbital libraries were set up to sample 25 equipotential shells at radii logarithmically spaced from $0''.006$ to $294''$, with 8 angular and 8 radial values at each energy to cover the three integrals of motion. We bundle together 5^3 orbits with adjacent starting positions and sum their observables, resulting in a total of 600,000 orbits. Such orbital dithering is commonly used in the construction of Schwarzschild models to ensure a smooth distribution function, and further smoothing can be applied after the linear orbital superposition through the adoption of a regularization term. Our results presented in §8 are based upon models run without regularization, however we note that including a small amount of regularization did not change the

best-fit black hole mass.

We estimate the model fitting uncertainty on M_{BH} (M/L) by marginalizing over M/L (M_{BH}) and the shape parameters. Following Cappellari et al. (2009) and Krajnović et al. (2009), who advise the use of 3σ errors for M_{BH} measurements due to the numerical uncertainties associated with Schwarzschild modeling, we quote the 3σ uncertainties on M_{BH} and M/L for one degree of freedom. This corresponds to a change of 9.0 in χ^2 from the minimum value. The statistical uncertainties on the intrinsic shape parameters are derived differently, using the confidence levels established by van den Bosch & van de Ven (2009) and applied during the studies of M32 and NGC 3379 by van den Bosch & de Zeeuw (2010). The confidence interval for the intrinsic shape parameters are set based upon the expected standard deviation in χ^2 , or $\sqrt{2N_{\text{obs}}}$, where N_{obs} is the number of observables used to constrain the model (1072 for NGC 3998). While the M_{BH} determination is influenced by the innermost kinematical measurements, the intrinsic shape parameters are set by a much larger number of observables, such that the expected scatter in χ^2 becomes important and is much larger than the standard $\Delta\chi^2$ criterion (van den Bosch & van de Ven 2009).

8. RESULTS

It is computationally prohibitive to explore parameter space for the full range of M_{BH} , M/L , p , q , and u values simultaneously, so we initially fixed M_{BH} and varied M/L and the shape parameters. We sampled axis ratios of $0.60 \leq p \leq 1.00$, $0.40 \leq q \leq 0.88$, and all possible values of u in steps of 0.06, and evaluated 11 I -band M/L values between 4.16 and 6.24 M_{\odot}/L_{\odot} . The minimum values of p and q were chosen to reflect the smallest values that have been observed in other galaxies as well as to probe very triaxial shapes, and the upper bound on q was set by the average flattening of 2D Gaussians in the MGE model for NGC 3998. With our sampling, we have covered 128 different galaxy shapes, 5 of which are oblate axisymmetric. This procedure assumes that the shape

parameters do not depend on the black hole mass, which was shown to be true for the specific cases of M32 and NGC 3379 (van den Bosch & de Zeeuw 2010). We tested whether this also holds for NGC 3998 by first setting $M_{\text{BH}} = 2.2 \times 10^8 M_{\odot}$ [the de Francesco et al. (2006) gas dynamical black hole mass measurement adjusted for our assumed distance], and then using a larger mass of $M_{\text{BH}} = 7.9 \times 10^8 M_{\odot}$ [the mass predicted from the $M_{\text{BH}} - \sigma_*$ relationship when a bulge stellar velocity dispersion of 305 km s^{-1} is assumed (Gültekin et al. 2009b)]. We found that the best-fit intrinsic shapes differ for the two M_{BH} values tested: an oblate axisymmetric shape, with $p = 1.00$ and $q = 0.81$ at an effective radius (R_e) is preferred when $M_{\text{BH}} = 2.2 \times 10^8 M_{\odot}$, and a round, but triaxial shape, with $p = 0.91$ and $q = 0.81$ at $1 R_e$ is found when $M_{\text{BH}} = 7.9 \times 10^8 M_{\odot}$.

Given that the best-fit intrinsic shape changes with M_{BH} , we constructed a model grid by varying M_{BH} between 5.0×10^7 and $5.0 \times 10^9 M_{\odot}$ and examining 11 I -band M/L values between 4.2 and $6.2 M_{\odot}/L_{\odot}$, while also sampling ten shapes. These shapes have the lowest ten χ^2 values from the two grid runs described above, and they fully encompass the 3σ uncertainties of p , q , and u when M_{BH} is set to 2.2×10^8 and $7.9 \times 10^8 M_{\odot}$. We therefore should be covering the range of possible shapes for NGC 3998 during our search for the best-fit M_{BH} and M/L parameters.

The results of our dynamical models are summarized by Figure 7, which displays the contours of χ^2 as a function of M_{BH} and M/L after marginalizing over galaxy shape. The best model has a χ^2 of 1600, corresponding to a χ^2 per degree of freedom (χ^2_{ν}) of 1.5, with $M_{\text{BH}} = (8.1^{+2.0}_{-1.9}) \times 10^8 M_{\odot}$, I -band $M/L = 5.0^{+0.3}_{-0.4} M_{\odot}/L_{\odot}$, and an intrinsic shape described by $p = 0.96$ and $q = 0.81$ at $1 R_e$. The M_{BH} and M/L errors represent the 3σ statistical uncertainties, and the errors for the shape parameters will be discussed below. The kinematics predicted from such a model are compared to the observed OSIRIS, STIS, and LRIS data in Figures 8, 9, and 10, respectively. We additionally compare the OSIRIS velocity dispersions to those predicted from models with the best-fit mass of $M_{\text{BH}} = 8.1 \times 10^8 M_{\odot}$, a smaller black hole with $M_{\text{BH}} = 1.3 \times 10^8 M_{\odot}$, and a larger black hole with $M_{\text{BH}} = 3.6 \times 10^9 M_{\odot}$ in Figure 11. This figure demonstrates that our best-fit black hole mass is a reasonable one, and clear differences between the predicted velocity dispersions for the models with a smaller and larger black hole and the observed kinematics can be seen by eye. The more massive black hole produces velocity dispersions that are much too large at the center, while the smaller black hole is unable to match the sharp rise in the observed nuclear velocity dispersion.

We calculated another model grid holding M_{BH} fixed at $M_{\text{BH}} = 8.1 \times 10^8 M_{\odot}$ and allowing M/L and the shape parameters to vary. This grid allowed us to derive the uncertainties on the shape parameters, having previously determined the best-fit black hole mass. We again sampled 128 galaxy shapes with axis ratios of $0.60 \leq p \leq 1.00$, $0.40 \leq q \leq 0.88$, and all possible values of u , and examined 11 I -band M/L values between 4.2 and $6.2 M_{\odot}/L_{\odot}$. We found that the galaxy shape can be described with the ratios $p = 0.96^{+0.04}_{-0.13}$ and $q = 0.81^{+0.00}_{-0.33}$ (3σ uncertainties) at $1 R_e$. In Figure 12, we plot the best-fit axis ratios p and q and their uncertainties at all radii, extending out to $100''$. We further show the radial variation of the triaxiality parameter, $T = (1 - p^2)/(1 - q^2)$, on the same plot. An upper error bar of zero is measured for q because this ratio is lim-

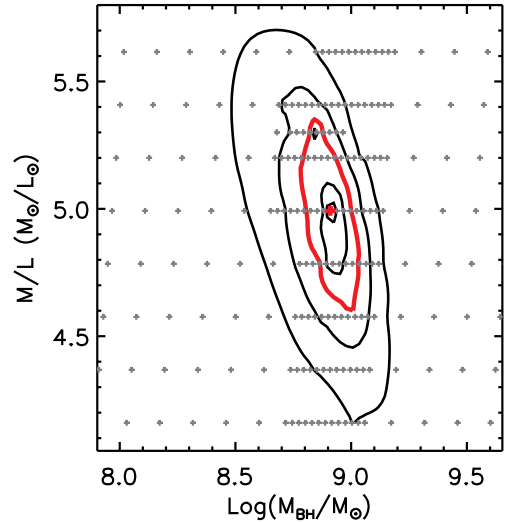


FIG. 7.— Results of the stellar dynamical models after marginalizing over the intrinsic shape of the galaxy. At each grey cross, a dynamical model was calculated for the specified combination of black hole mass and I -band M/L , and the red cross marks the best-fit model. Overplotted are contours of $\Delta\chi^2$, with the inner two contours denoting the 1σ and 2σ confidence levels, and the thick red contour signifying the 3σ interval for one degree of freedom. Contours beyond the 3σ confidence level are separated by a factor of two.

ited by the observed average flattening of the 2D Gaussians from the MGE model. Thus, the best-fit intrinsic shape is as round as the *HST*/CFHT images allow, and is consistent with an oblate axisymmetric spheroid. Furthermore, we were unable to place strong constraints on the viewing angles, finding that the inclination ranges from $\theta = 38^\circ$ to $\theta = 90^\circ$ (edge-on), $\phi = -90^{+82}_{-0}$, and $\psi = 90^{+0}_{-4}$ (3σ uncertainties). These results are consistent with previous stellar dynamical studies of other early-type galaxies, in particular the work of Krajnović et al. (2005) and van den Bosch & van de Ven (2009) who find that the viewing angles are highly degenerate.

8.1. Additional Sources of Uncertainty

The 3σ errors on M_{BH} presented above represent the formal model fitting uncertainty, and account for the random noise within the stellar dynamical models. We further explored other sources of uncertainty that are not included in the statistical errors but that could have an effect the M_{BH} determination. We summarize the results of these model grids below.

Stellar Density Distribution: Care must be taken to separate the AGN light from the stellar contribution when constructing the luminous mass model. Often, this is accomplished by removing the innermost Gaussian component from the MGE model, however NGC 3998 exhibits a steep surface brightness profile and some starlight may still be contained within the central component. In the analysis presented above, we assumed that all of the light from the central MGE Gaussian was due to the stars. Here, we consider the other extreme, where all the light from the inner MGE component comes from the AGN.

After removing the central Gaussian component from the MGE model, we followed the same procedure outlined in §8. We first calculated stellar dynamical models fixing M_{BH} to $2.2 \times 10^8 M_{\odot}$ and $7.9 \times 10^8 M_{\odot}$ in order to determine the most

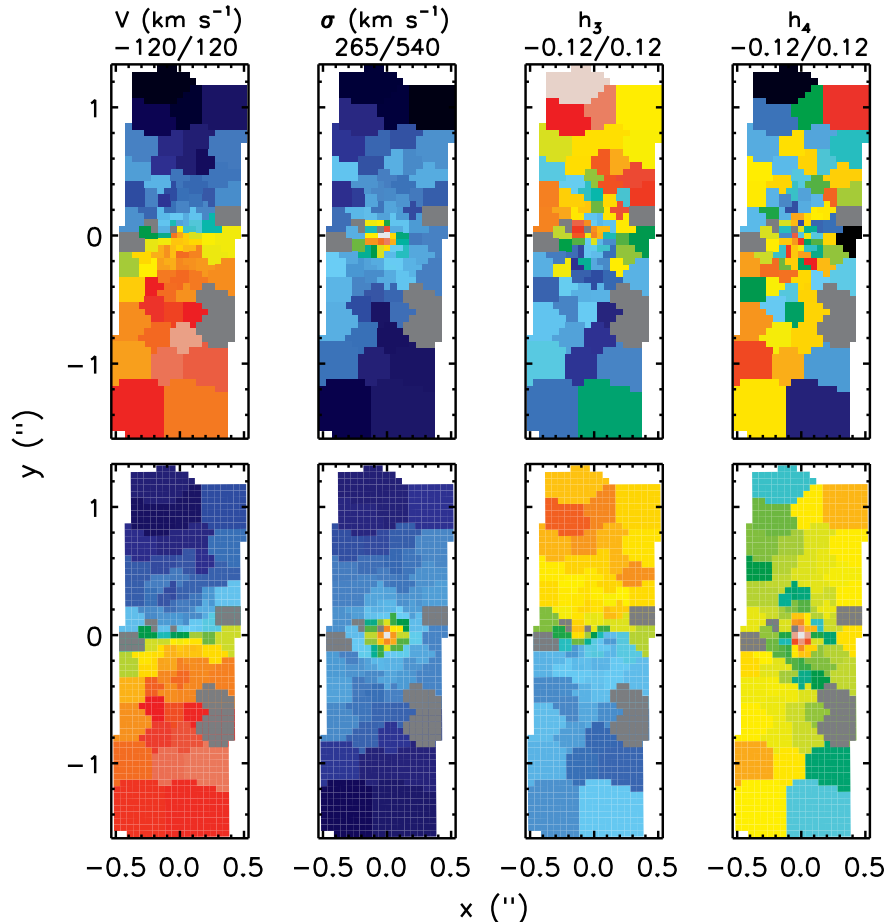


FIG. 8.— The stellar kinematics measured for NGC 3998 from the OSIRIS data (top panels) and the predicted values (bottom panels) from the best-fit stellar dynamical model with $M_{\text{BH}} = 8.1 \times 10^8 M_{\odot}$, I -band $M/L = 5.0 M_{\odot}/L_{\odot}$, and a shape described by $p = 0.96$ and $q = 0.81$ at $1 R_e$. The velocity map shows that the galaxy is rotating rapidly, the velocity dispersion map displays a sharp peak within the inner $0''.1$, and the h_3 map is anti-correlated with the velocity map. The long axis of the IFU was aligned with the major axis of the nuclear gas disk at a position angle of 308° , thus the top of the maps correspond to the northwest side of the galaxy. The data and model maps are plotted on the same scale, with the ranges given by the color bar to the right and the minimum and maximum values printed at the top of the maps. The kinematics measured from the bins in dark grey were deemed unreliable, and were excluded from the subsequent stellar dynamical modeling.

probable galaxy shapes. Then, we ran model grids sampling over the ten best galaxy shapes, while varying M_{BH} between 5.0×10^7 and $5.0 \times 10^9 M_{\odot}$ and M/L between 4.2 and $6.2 M_{\odot}/L_{\odot}$. We found a very round, but oblate, intrinsic shape for the galaxy, with $M_{\text{BH}} = (10.1_{-3.5}^{+0.7}) \times 10^8 M_{\odot}$ and an I -band $M/L = 4.8_{-0.1}^{+0.6} M_{\odot}/L_{\odot}$ (3σ uncertainties). This best-fit stellar dynamical model is a worse description of the observations ($\chi^2 = 1619$) compared to the best model presented previously in §8 ($\chi^2 = 1600$). Moreover, when excluding the central MGE component, the dynamical models for every combination of M_{BH} and M/L have a higher χ^2 than the stellar dynamical models constructed from a mass model with all 12 Gaussian components. For this reason, and because the black hole masses determined using the two MGE models are fully consistent within the statistical uncertainties, covering nearly identical M_{BH} ranges, we view the best-fit model from §8 as our final result.

Dark Halo: Work by Gebhardt & Thomas (2009) has raised concerns that stellar dynamical black hole mass measurements may be underestimated if both the black hole and the dark matter halo are not simultaneously modeled. The reasoning is that without a dark halo, the M/L may be overestimated

in order to compensate for the missing mass at large radii. The M/L is assumed to be constant in the models, and thus a smaller black hole would be needed to match the observed nuclear kinematics. By including the contribution of dark matter in their re-examination of M87, Gebhardt & Thomas (2009) found that the black hole mass increased by about a factor of two. Likewise, McConnell et al. (2011a) noted a strong dependence of the black hole mass on the dark halo when studying NGC 6086. Both objects exhibit shallow stellar luminosity profiles and have massive, concentrated dark matter halos, limiting the radial range over which the stars dominate the gravitational potential and the assumption of a constant M/L holds. Moreover, these studies utilized data in which the quality and/or spatial resolution was unable to limit the degeneracy between the black hole and stellar mass-to-light ratio in the central regions. In contrast, black hole mass measurements based upon high S/N observations well within the region influenced by the black hole appear to be less sensitive to the inclusion of dark halos during the modeling (Shen & Gebhardt 2010; Schulze & Gebhardt 2011; Gebhardt et al. 2011).

We are unable to directly fit for the parameters of a dark

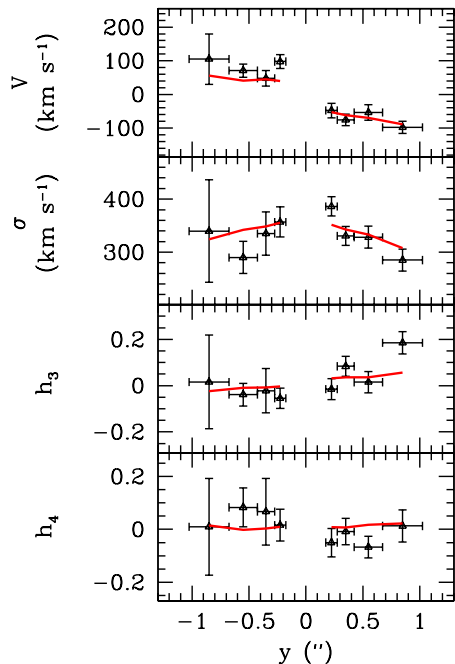


FIG. 9.— The observed STIS kinematics (black) and the predicted kinematics (red line) from the best-fit dynamical model. The velocity, velocity dispersion, h_3 , and h_4 are plotted as a function of position, relative to the nucleus, along the STIS slit. The slit was aligned with the galaxy’s major axis. We were unable to measure the stellar kinematics within $\sim 0''.2$ of the nucleus due to AGN contamination, and model predictions were not generated for this region. The kinematics are similar to those measured from the OSIRIS data.

halo model because our kinematics do not extend out to large enough radii. Instead, we selected a fixed model for the dark halo. Two commonly used dark halo models are the Navarro-Frenk-White (NFW) profile (Navarro et al. 1996) and a distribution based on a cored logarithmic potential (Binney & Tremaine 1987; Thomas et al. 2005). Previous work has found that both parameterizations give consistent results (Thomas et al. 2007; Gebhardt & Thomas 2009; McConnell et al. 2011a), and here we adopt the profile from a logarithmic potential given by

$$\rho_{\text{DM}}(r) = \frac{V_c^2}{4\pi G} \frac{3r_c^2 + r^2}{(r_c^2 + r^2)^2}. \quad (1)$$

The parameters V_c and r_c are the asymptotically constant circular velocity and the core radius, within which the dark matter density is approximately constant. We fixed V_c and r_c to values of 407 km s^{-1} and 10.7 kpc , respectively, which were chosen for NGC 3998 using the galaxy B -band luminosity of $1.6 \times 10^{10} L_\odot$ reported by the Hyperleda database (Paturel et al. 2003) and the empirical relations by Thomas et al. (2009). The relationships in Thomas et al. (2009) provide a way to select physically motivated parameters for the dark matter halo, and was similarly used by Schulze & Gebhardt (2011) to test the effects of dark matter on the black hole mass.

When including the dark halo in our stellar dynamical models, we did not observe a significant change in the black hole mass, measuring $M_{\text{BH}} = (7.1_{-0.9}^{+3.7}) \times 10^8 M_\odot$ and an I -band $M/L = 5.0_{-0.4}^{+0.2} M_\odot/L_\odot$ (3σ errors). The decrease in the best-

fit black hole mass is in the opposite direction as anticipated, but is well within the statistical uncertainties and is likely due to noise in the dynamical models. A similar result was seen when we incorporated a dark halo that was twice as massive within the radial range covered by the large-scale LRIS kinematics. Therefore, neglecting the dark matter contribution during the dynamical modeling presented in §8 did not lead to a biased M_{BH} determination. We attribute this result to the high quality OSIRIS data, which probes regions well within the influence of the black hole and reduces the degeneracy between M_{BH} and M/L , as well as to the galaxy’s strong rotation, which also makes the measurement less sensitive to the dark halo.

Central OSIRIS Kinematics: Contributions from a non-stellar nucleus dilute absorption lines and make the measurement of reliable stellar kinematics challenging. In some instances, the AGN contribution is so strong that the stellar features are no longer visible in the nuclear spectra (Cappellari et al. 2009). This is not the case for NGC 3998, however we do measure large errors for the kinematics extracted from four of innermost OSIRIS lenslets. As an example, at these locations we found velocity dispersions between 500 and 560 km s^{-1} with error bars of $42 - 146 \text{ km s}^{-1}$. Beyond these four lenslets, but still within $\sim 0''.1$ of the nucleus, we continued to measure large velocity dispersions of $\sigma \sim 450 \text{ km s}^{-1}$ but with more reasonable errors of $\sim 20 \text{ km s}^{-1}$. The large uncertainties from the inner OSIRIS bins indicate that the pPXF routine could not model the AGN contribution in a consistent fashion within $0''.05$ from the nucleus, which in turn may have biased these kinematical measurements. Therefore, we excluded the measurements from the central five OSIRIS bins when fitting the orbit-based stellar dynamical models. Doing so led to a best-fit model with $M_{\text{BH}} = (8.1 \pm 2.0) \times 10^8 M_\odot$ and I -band $M/L = 5.0_{-0.4}^{+0.2} M_\odot/L_\odot$. The values and 3σ uncertainties for M_{BH} and M/L are the same as found previously in §8, when all of the OSIRIS kinematics were fit during the modeling. Even if the kinematics measured from four of the innermost OSIRIS lenslets are biased due to AGN contamination, there appears to be no subsequent effect on the black hole mass. This result is not entirely surprising because the stellar dynamical models take into account the errors on the input kinematics, and we have a number of other reliable measurements of the LOSVD within the black hole sphere of influence.

OSIRIS PSF: As discussed in §6, the OSIRIS PSF was determined by comparing the deconvolved HST WFPC2 F791W image to the OSIRIS K -band data cube summed along the wavelength axis. This approach assumes that the comparison image has a higher resolution than the collapsed data cube and that there is no strong color gradient. Given the difficulties associated with measuring the PSF, we therefore additionally considered two extreme parameterizations of the OSIRIS PSF to quantify changes in M_{BH} . Both PSFs were composed of two concentric, circular, 2D Gaussians, and the dispersion of the second component was set at $0''.28$. We chose $0''.28$ because this is the dispersion of the broad component in the OSIRIS PSF model presented in §6. We then constructed a “poor” PSF, such that the narrow component had a dispersion of $0''.084$ and contributed 15% of the flux to the total PSF, and a “good” PSF, whose narrow component had a dispersion of $0''.025$ (roughly the K -band diffraction limit for a 10m telescope) and contributed 95% of the flux to the total PSF. The stellar dynamical models based upon the “bad” PSF yielded

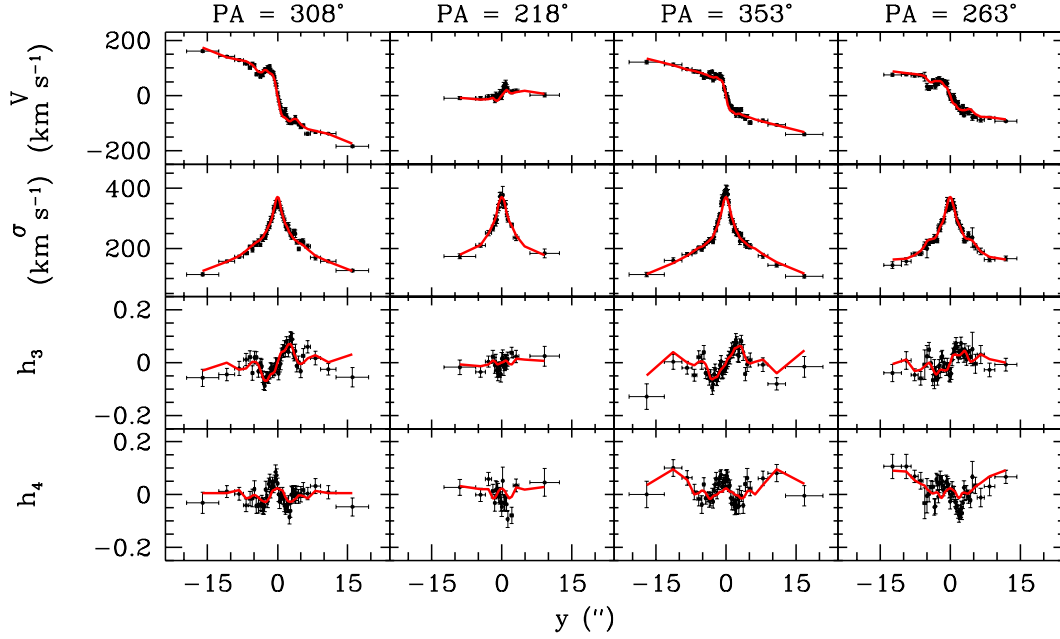


FIG. 10.— The observed LRIS kinematics (black) and predicted values from the best-fit dynamical model (red line). The LRIS observations were obtained at four position angles: along the major axis of the nuclear gas disk (PA = 308°), along the minor axis (PA = 218°), and at two intermediate angles (PA = 353° and PA = 263°). For each of the slit positions, the velocity, velocity dispersion, h_3 , and h_4 are plotted as a function of location along the slit relative to the nucleus. These large-scale kinematics exhibit similar features to those seen from the high angular resolution data, which include rapid rotation, a steep rise in the velocity dispersion, and an anti-correlation between h_3 and V . Furthermore, h_4 is symmetric about the center with a slight peak at the nucleus.

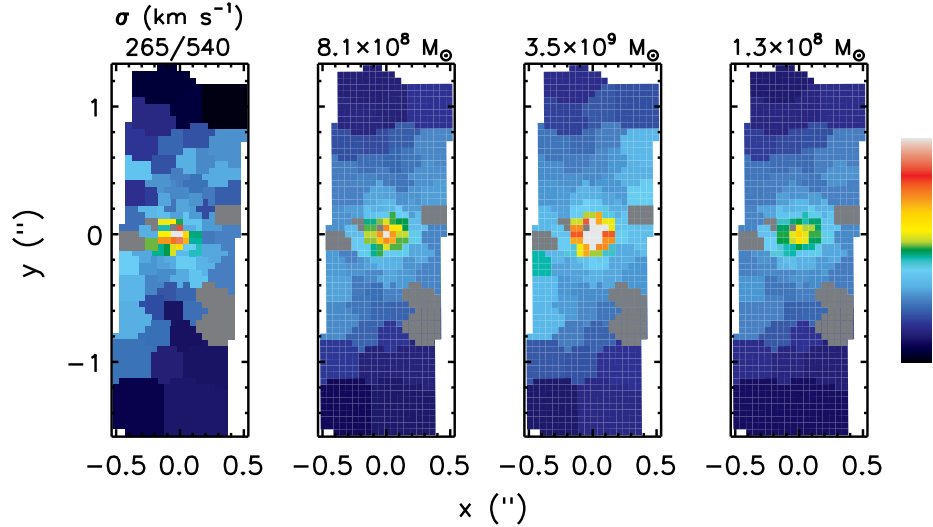


FIG. 11.— Comparison between the observed velocity dispersions over the OSIRIS field of view and the predicted ones for various dynamical models. The models were constructed with different black hole masses (the best-fit M_{BH} of $8.1 \times 10^8 M_{\odot}$, a larger black hole with $M_{\text{BH}} = 3.6 \times 10^9 M_{\odot}$, and a smaller black hole of $M_{\text{BH}} = 1.3 \times 10^8 M_{\odot}$), but have the same I -band M/L ($5.0 M_{\odot}/L_{\odot}$) and intrinsic shape ($p = 0.96$ and $q = 0.81$ at $1 R_e$). All maps are plotted on the same scale, given by the color bar to the right along with the minimum and maximum values listed on top of the left-most panel. Observed kinematics measured from the grey bins were deemed unreliable, and we do not show the model predictions in these bins.

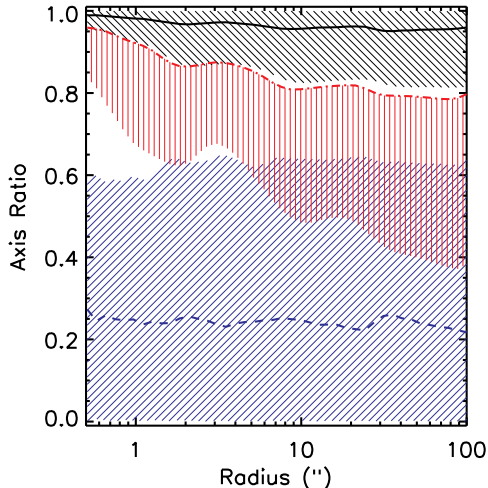


FIG. 12.— The intrinsic shape of NGC 3998. The ratio, p , between the intermediate and long axes (solid black line), the ratio, q , between the short and long axes (dash-dotted red line), and the triaxiality parameter T (dashed blue line) are plotted as a function of distance from the nucleus. The 3σ uncertainties are given by the range covered by the black backward, red vertical, and blue forward slashes for p , q , and T , respectively. The kinematical measurements from the large-scale LRIS data extend out to a radius of $\sim 15''$.

a best-fit model with $M_{\text{BH}} = (8.7^{+3.9}_{-1.6}) \times 10^8 M_{\odot}$ and I -band $M/L = 5.0^{+0.2}_{-0.4} M_{\odot}/L_{\odot}$, and the models using the “good” PSF produced best-fit parameters of $M_{\text{BH}} = (8.1^{+1.1}_{-1.4}) \times 10^8 M_{\odot}$ and I -band $M/L = 5.0 \pm 0.2 M_{\odot}/L_{\odot}$. Thus, even for two extreme PSF models, the black hole mass remains within the 3σ statistical uncertainties presented in §8.

Symmetrizing the Kinematics: We removed the systematic offsets in the odd Gauss-Hermite moments (e.g., the galaxy’s systemic velocity) with the point-symmetrization code of van den Bosch & de Zeeuw (2010). In addition to this step, the common practice is to make further adjustments to the kinematical measurements and their errors so that the velocity fields become bi- or point-symmetric, thereby reducing the observational noise. However, the symmetrization process assumes that the galaxy nucleus is centered on one of the lenslets, which is not necessarily true for the OSIRIS data. Therefore, in §8, we calculated stellar dynamical models without first requiring the observed velocity fields to be symmetric. Instead, if we do symmetrize the input kinematics, we find a best-fit model with $M_{\text{BH}} = (9.5^{+2.3}_{-3.2}) \times 10^8 M_{\odot}$ and an I -band $M/L = 4.8^{+0.4}_{-0.2} M_{\odot}/L_{\odot}$. As expected, the best model is a much better description of the (symmetrized) observed kinematics, with $\chi^2 = 459$ and $\chi^2_{\nu} = 0.43$, and larger statistical 3σ uncertainties on M_{BH} are found. Although the best-fit black hole mass increased by 17% from the mass derived previously, it remains within the model fitting uncertainties determined in §8, and we continue to prefer the dynamical model constrained with the non-symmetrized kinematics.

9. DISCUSSION

Through orbit-based stellar dynamical modeling we measured a mass of $M_{\text{BH}} = (8.1^{+2.0}_{-1.9}) \times 10^8 M_{\odot}$ for the black hole in NGC 3998. We report 3σ statistical errors on the black hole mass, but ran additional model grids to assess the robustness of our mass measurement. We found no significant changes (outside the random noise of the models) to the black hole

mass due to these sources of uncertainty, and so we do not make any additional adjustments to the black hole mass or its error bars. With this black hole mass, and a bulge stellar velocity dispersion of 272 km s^{-1} (see §9.3 below), the black hole sphere of influence is $r_{\text{sphere}} = 0''.7$, which is well resolved by the observations. We now examine the orbital structure of galaxy, compare the stellar dynamical black hole mass measurement to the existing gas dynamical mass, and place NGC 3998 on the $M_{\text{BH}} - \text{host galaxy}$ relationships.

9.1. Orbital Structure

We examined the internal orbital structure of NGC 3998 using the orbital weights found with the Schwarzschild superposition method for our best fitting model (presented in §8). Defining the tangential velocity dispersion as $\sigma_t^2 = (\sigma_{\phi}^2 + \sigma_{\theta}^2)/2$, with (r, θ, ϕ) being the usual spherical coordinates, we plot the ratio σ_r/σ_t as a function of radius in the top panel of Figure 13. Near the nucleus, the velocity dispersion becomes radially anisotropic reaching values of $\sigma_r/\sigma_t \sim 1.5$, while the velocity dispersion is isotropic, deviating by at most $\sim 10\%$ from $\sigma_r/\sigma_t = 1$, at radii beyond $\sim 0''.1$. The radial anisotropy near the galaxy’s center can be attributed to the large fraction of box orbits: we found that the box orbits contribute 60–80% to the stellar mass within the inner $\sim 0''.1$ (see bottom panel of Figure 13). Similarly large contributions from box orbits have been seen when applying triaxial Schwarzschild models to other objects as well (Weijmans et al. 2009; van den Bosch & de Zeeuw 2010). Outside of r_{sphere} , our best-fit model is made up of $\sim 65\%$ short-axis tube orbits and $\sim 20\%$ long-axis tube orbits.

NGC 3998 is classified as an S0 galaxy, and indeed, our best fitting dynamical model shows evidence for both a bulge and a disk component. In Figure 14, we show the mass distribution along orbits as a function of average radius and spin, $\bar{\lambda}_z$. The spin is defined as $\bar{\lambda}_z = \bar{J}_z / (\bar{r}/\bar{\sigma})$, where \bar{J}_z is the average angular momentum along the z -direction, \bar{r} is the average radius, and $\bar{\sigma}$ is the average second moment of the orbit. The figure shows the clear presence of a non-rotating bulge component ($-0.2 < \bar{\lambda}_z < 0.2$) and a rotating disk component ($\bar{\lambda}_z \geq 0.2$), making up 52% and 39% of the mass within the radial range covered by our kinematic measurements. The remaining 9% of the mass comes from orbits with $\bar{\lambda}_z \leq -0.2$ that fall outside the radial range covered by the OSIRIS kinematics. Thus, the near isotropy at radii larger than $\sim 0''.1$ seen in Figure 13 is due to the presence of a bulge component, while the disk causes the strong rotation that is seen in the OSIRIS, STIS, and LRIS kinematics in Figures 8, 9, and 10.

9.2. Comparison to the Gas Dynamical Measurement

By modeling the *HST* STIS gas kinematics as a thin, circularly rotating disk, de Francesco et al. (2006) derived a black hole mass of $M_{\text{BH}} = (2.7^{+2.4}_{-2.0}) \times 10^8 M_{\odot}$ (2σ uncertainties). Scaling the black hole mass for the distance adopted here, their mass measurement becomes $M_{\text{BH}} = (2.2^{+1.9}_{-1.6}) \times 10^8 M_{\odot}$. The stellar dynamical black hole mass is therefore significantly larger, by nearly a factor of four, compared the gas dynamical measurement. We cannot resolve the discrepancy between the stellar and gas dynamical mass measurements for the black hole in NGC 3998, but discuss a few of the uncertainties associated with both methods below.

The gas kinematics measured from the STIS data clearly show organized rotation. However, the line widths predicted from a rotating, dynamically cold, thin-disk model

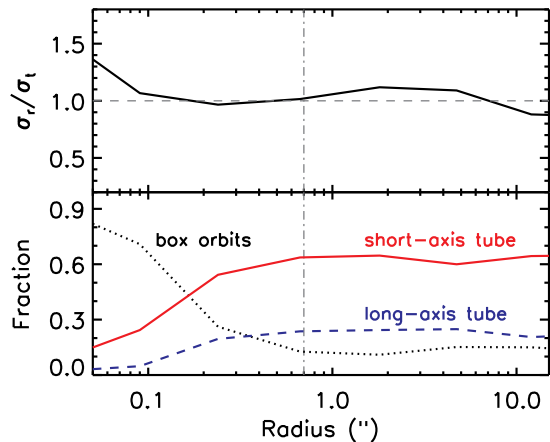


FIG. 13.— Orbital structure of NGC 3998 from our best fitting stellar dynamical model. The anisotropy, σ_r/σ_t , (top) and the orbit type (bottom) are plotted as a function of radius, covering the extent of the kinematic measurements. The vertical grey dot-dashed line designates the black hole sphere of influence. NGC 3998 is mostly isotropic (indicated by the horizontal dashed grey line in the top panel) but shows a radial bias within $\sim 0''.1$. Near the nucleus, box orbits (black dotted line) dominate the galaxy, while short-axis tube orbits (red solid line) become important at larger radii. Long-axis tube orbits are shown by the blue dashed line.

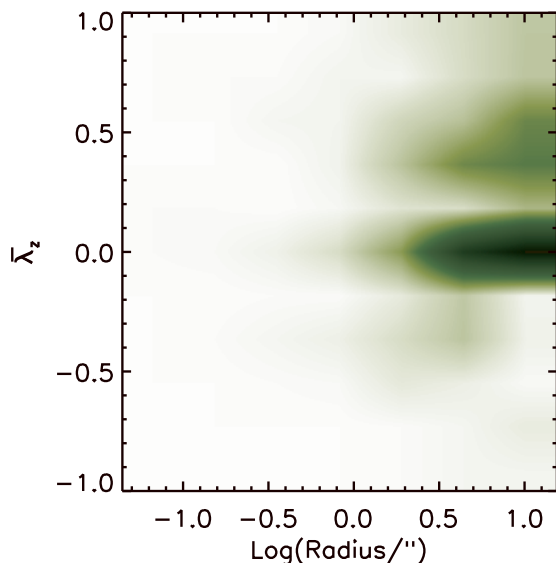


FIG. 14.— Distribution of mass along the orbits from our best fitting dynamical model as a function of average radius and spin. The radial range extends over the region covered by our kinematic measurements. A non-rotating bulge ($-0.2 < \bar{\lambda}_z < 0.2$) and rotating disk ($\bar{\lambda}_z \geq 0.2$) component are clearly present.

do not fully match the observed velocity dispersions. de Francesco et al. (2006) found that the model underestimates the observed rise in the nuclear velocity dispersion by $\sim 20\%$, although larger inconsistencies were seen in the two slit positions immediately adjacent to the central slit. Without re-analyzing the STIS data for NGC 3998, it is difficult to determine whether the addition of an intrinsic velocity dispersion to the models would greatly improve the agreement between the predicted and observed line widths, and by how

much the gas dynamical black hole mass measurement would then increase if the excess velocity dispersion was considered dynamically important. Previous gas dynamical studies that have assigned a dynamical origin to the internal velocity dispersion have found varying degrees to which the black hole mass is affected. For example, using an asymmetric drift correction to estimate the circular velocity from the observed mean rotational speed, Barth et al. (2001) found a 12% increase in the best-fit black hole mass for NGC 3245 while Walsh et al. (2010) found that the mass of the black hole in M84 doubles. However, we note that the differences between the observed line widths and the predictions from a dynamically cold, rotating disk model for NGC 3245 and M84 were larger than those observed for NGC 3998. Admittedly, the factor of four increase needed to make the best-fit gas dynamical mass to match the best-fit stellar dynamical measurement is quite large, and the discrepancy probably cannot be entirely resolved by assigning a dynamical origin to an intrinsic velocity dispersion.

Another source of uncertainty in the gas dynamical black holes mass comes from the inclination of the emission-line disk. de Francesco et al. (2006) found that all models with inclinations below 70° produced equally acceptable fits to the data at the 2σ level, and that the inferred black hole masses differed by about an order of magnitude for inclination angles $i = 10^\circ$ and 70° . A similarly large difference in the NGC 3998 black hole mass for extreme inclination angles was reported by Beifiori et al. (2009), who estimated masses of $M_{\text{BH}} = 3.4 \times 10^8 M_\odot$ and $4.9 \times 10^7 M_\odot$ (adjusted to our distance) for inclinations of $i = 33^\circ$ and 88° . de Francesco et al. (2006) ruled out very face-on orientations, $i < 27^\circ$, because such angles produced V-band mass-to-light ratios that are too high compared the predictions of a Salpeter initial mass function (IMF) for an old stellar population. They ultimately reported results using a disk inclination of 30° , and further combined their statistical uncertainties on M_{BH} with the uncertainties resulting from the allowed range in inclination angles between 27° and 70° to derive the 2σ error bars on M_{BH} . Interestingly, the results of Cappellari et al. (2012) indicate that the most massive galaxies have M/L values that are higher than the predictions of a Salpeter IMF for an old stellar population, thus lower inclinations of the gas disk in NGC 3998 may be acceptable, which would then lead to an increase in the gas dynamical mass measurement.

When constructing the stellar dynamical models presented here, we did not assume axisymmetry or a specific viewing orientation. However, it is not feasible to explore all possible values for the five parameters simultaneously, and we employed a method that begins by holding fixed M_{BH} while varying the other parameters to find the best-fit intrinsic galaxy shape before searching for the best-fit M_{BH} . Such an approach does not guarantee that a global minimum will be found, and we attempted to alleviate this problem by sampling over ten galaxy shapes (instead of just the best-fit shape) while varying M_{BH} and M/L . The ten shapes were taken from the ten best models when M_{BH} was held at two different values, and the shapes cover the 3σ ranges of p , q , and u for the two black hole masses. Thus, we should have covered the possible galaxy shapes while searching for the best fitting M_{BH} and M/L parameters.

One assumption that is made when constructing the stellar dynamical models is that the M/L does not vary with radius. NGC 3998 has both bulge and disk components, and could

also contain a nuclear star cluster (González Delgado et al. 2008; Neumayer & Walcher 2012). If each of these components has a very different stellar population, then a single M/L is not a realistic description of the system. Recent work (e.g., van Dokkum & Conroy 2010) has advocated for a bottom-heavy IMF in massive early-type galaxies. Thus, if the bulge component of NGC 3998 is indeed rich in dwarf stars, the larger M/L for the bulge region would lead to a smaller stellar dynamical black hole mass measurement. However, allowing for a radial variation in M/L , in addition to sampling the M_{BH} and three shape parameters, is too computationally expensive to be attempted here. In contrast, the gas dynamical black hole mass measurement, which relies on the gas kinematics at small radii where the stellar potential is dominated by the bulge, is insensitive to M/L variations. While our assumption of a constant M/L , may effect the derivation of the stellar dynamical black hole mass, the other systematic effects often associated with the stellar dynamical method appear to be minimal. For example, we found the black hole mass was insensitive to the inclusion of a dark halo in the model, as well as to the exact OSIRIS PSF that was adopted. Moreover, we found good agreement between the kinematics measured from different instruments using different template libraries, suggesting that template mismatch is not a dominant source of uncertainty.

9.3. The Black Hole Scaling Relations

When placing NGC 3998 on the $M_{\text{BH}} - \sigma_*$ relation, Gültekin et al. (2009b) adopted a bulge stellar velocity dispersion of 305 km s^{-1} . The value was taken from the Hyperleda database, and was based upon the dispersion values found in the literature at that time, however we are in a position to directly measure the effective stellar velocity dispersion (σ_e) of the bulge component from our data and models. Recent studies of very massive black holes have elected to exclude data within r_{sphere} when measuring the effective velocity dispersion (Gebhardt et al. 2011; Jardel et al. 2011; McConnell et al. 2011b), and here we follow the same approach. We weight the σ and V measurements obtained from the LRIS major axis slit with the surface brightness profile set by our MGE model, following Gültekin et al. (2009b), but integrate from r_{sphere} to the bulge effective radius. The bulge effective radius is rather uncertain for NGC 3998, with literature values ranging between $4.''7 < R_e < 18.''3$ (Sani et al. 2011; Baggett et al. 1998), which in turn produces some uncertainty in the measurement of σ_e . Taking an average of the R_e measurements determined from recent optical images (Fisher et al. 1996; Sánchez-Portal et al. 2004), we find that $R_e = 10.''7$ and $\sigma_e = 272 \text{ km s}^{-1}$ for NGC 3998. For comparison, effective stellar velocity dispersions of $\sigma_e = 282 \text{ km s}^{-1}$ and 270 km s^{-1} are measured for $R_e = 4.''7$ and $18.''3$, respectively. We note, however, that there is just a single measurement of the large-scale stellar kinematics on each side of the nucleus beyond a radius of $12.''$, making it difficult to determine σ_e for a bulge effective radius of $18.''3$ from the LRIS data.

These σ_e measurements are based upon the large-scale kinematics extracted from the major axis LRIS slit, however the best-fit stellar dynamical model from §8 allows us to predict the luminosity-weighted second moment from a circular aperture of radius R_e . We measured an effective velocity dispersion of $\sigma_e = 239 \text{ km s}^{-1}$ when a bulge effective radius of $R_e = 10.''7$ is used and the central regions within r_{sphere} are ex-

cluded. This method provides a formally more correct estimate of σ_e , as a circular aperture is being considered instead of relying on a single slit position, but most of stellar velocity dispersions on the $M_{\text{BH}} - \sigma_*$ relationship were derived using long-slit data and the definition given by Gültekin et al. (2009b). Thus, for consistency purposes we continue to consider the measurements of σ_e made from the LRIS data.

With an effective stellar velocity dispersion of $\sigma_e = 272 \text{ km s}^{-1}$, the black hole mass predicted from the $M_{\text{BH}} - \sigma_*$ relation is $9.4 \times 10^8 M_\odot$ using the recent calibration of McConnell et al. (2011b). Instead, black hole masses of $6.5 \times 10^8 M_\odot$ and $4.9 \times 10^8 M_\odot$ are predicted from the $M_{\text{BH}} - \sigma_*$ correlation calibrated by Graham et al. (2011) and Gültekin et al. (2009b). Thus, our stellar dynamical black hole mass measurement falls within the expectations of the relationship when calculating σ_e using the large-scale LRIS kinematics and a bulge effective radius of $10.''7$.

To place NGC 3998 on the $M_{\text{BH}} - L_{\text{bul}}$ correlation, we use the total, extinction corrected, V -band luminosity of $9.7 \times 10^9 L_\odot$ for NGC 3998 from the Third Reference Catalog of Bright Galaxies (RC3; de Vaucouleurs et al. 1991). The average of the bulge-to-total ratio (B/T) values reported by Fisher et al. (1996) and Sánchez-Portal et al. (2004) is $B/T = 0.77$, which suggests a V -band luminosity of $7.5 \times 10^9 L_\odot$ for the bulge of NGC 3998. Such a bulge luminosity translates into a prediction of $7.2 \times 10^7 M_\odot$ and $5.0 \times 10^7 M_\odot$ for the black hole mass using the V -band $M_{\text{BH}} - L_{\text{bul}}$ relation of McConnell et al. (2011b) and Gültekin et al. (2009b). Even when deliberately overestimating the bulge luminosity, and using the total, V -band luminosity reported in RC3, the $M_{\text{BH}} - L_{\text{bul}}$ relation suggests a black hole mass of $9.6 \times 10^7 M_\odot$ (McConnell et al. 2011b). The stellar dynamical measurement therefore places NGC 3998 well above the $M_{\text{BH}} - L_{\text{bul}}$ relationship. In Figure 15, we show the location of NGC 3998 on the black hole mass scaling relations.

10. CONCLUSIONS

To conclude, we have studied the stellar dynamics of the nearby, S0 galaxy, NGC 3998. From Keck LGS AO OSIRIS observations in the K band and archival *HST* STIS data covering the Ca II triplet lines, we mapped out the 2D kinematics within $\sim 2.''$ of the nucleus with a superb angular resolution of $\sim 0.''1$, thereby resolving the gravitational sphere of influence of the black hole. In addition, we obtained long-slit data at four PAs with Keck LRIS to measure the large-scale stellar kinematics, extending to $\sim 1 R_e$, which is essential for constraining the stellar orbital distribution. We found that the galaxy is rapidly rotating with $V \sim \pm 200 \text{ km s}^{-1}$ and exhibits a very sharp rise in the velocity dispersion to values of $\sigma \sim 500 \text{ km s}^{-1}$. Our high-quality spectroscopic data further allowed us to quantify the LOSVD's asymmetric and symmetric deviations from a Gaussian through the h_3 and h_4 Gauss-Hermite moments. We observed an anti-correlation between h_3 and V , and slight peak in h_4 at the center from the large-scale data.

Combining the kinematics with the luminosity density measured from a *HST* WFPC2 F791W image and a CFHT WIRCam K_s image, we constructed three-integral, triaxial, Schwarzschild models. The intrinsic shape of the galaxy is very round (as round as the imaging observations allow), and oblate, with axis ratios $p = 0.96^{+0.04}_{-0.13}$ and $q = 0.81^{+0.00}_{-0.33}$ at a radius of $10.''7$. Although we are unable to place strong constraints on the shape parameters/viewing orientation, by sampling over them, we were able to extract a robust measurement

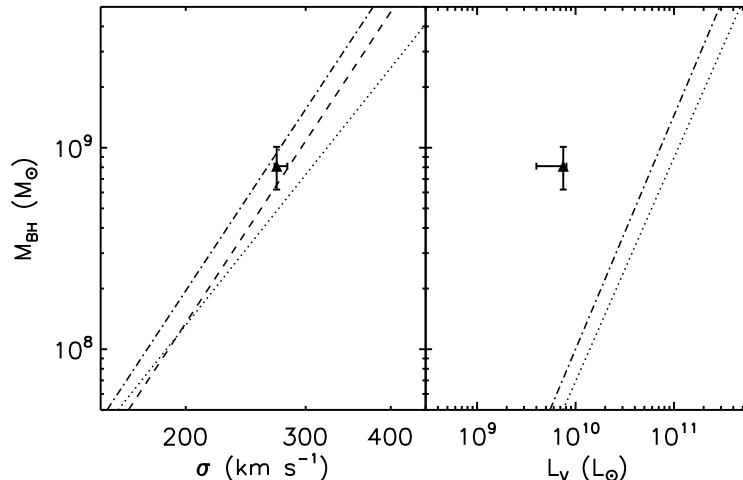


FIG. 15.— Location of NGC 3998 on the $M_{\text{BH}} - \sigma_*$ (left) and V-band $M_{\text{BH}} - L_{\text{bul}}$ (right) relationships. The correlations calibrated by Gültekin et al. (2009b), Graham et al. (2011), and McConnell et al. (2011b) are given by the dotted, dashed, and dot-dashed lines, respectively. The errors on the bulge stellar velocity dispersion show the range of values that were calculated using the large-scale LRIS data between r_{sphere} and the largest and smallest bulge effective radius measurements found in the literature [$R_e = 18''3$ (Baggett et al. 1998) and $R_e = 4''7$ (Sani et al. 2011)]. Similarly, the errors on the bulge luminosity were determined by applying the smallest and largest values of B/T found in the literature [$B/T = 0.41$ (Sani et al. 2011) and $B/T = 0.83$ (Sánchez-Portal et al. 2004)] to the total V-band luminosity given in RC3.

of the black hole mass and I -band stellar mass-to-light ratio, finding $M_{\text{BH}} = (8.1^{+2.0}_{-1.9}) \times 10^8 M_{\odot}$ and $M/L = 5.0^{+0.3}_{-0.4} M_{\odot}/L_{\odot}$. Additional model grids were run to assess possible systematic effects. We tested the effect on the black hole mass when assigning all the light from the central MGE component to the AGN, incorporating a fixed dark halo model, excluding the central OSIRIS kinematics that may be biased due to AGN contamination, adopting two extreme models for the OSIRIS PSF, and symmetrizing the kinematic measurements. We did not see any significant changes (outside of the modeling fitting uncertainties) to the best-fit M_{BH} or M/L .

With the stellar dynamical black hole mass measurement, NGC 3998 is consistent with $M_{\text{BH}} - \sigma_*$ when using a bulge stellar velocity dispersion of 272 km s^{-1} , but well off the $M_{\text{BH}} - L_{\text{bul}}$ correlation, even when overestimating the bulge luminosity. Also, the stellar dynamical black hole mass measurement is larger than the existing gas dynamical measurement, with the masses differing by close to a factor of four. NGC 3998 is now one of eight galaxies for which both stellar and gas dynamical modeling have been used to measure the mass of the central black hole. However, the gas kinematics turned out to be strongly disturbed in two of the galaxies and a clear best-fit mass and the associated uncertainties could not be measured for another object, preventing a meaningful comparison between the stellar and gas dynamical techniques. The five remaining comparison studies have produced mixed results, ranging from excellent agreement between the two mass measurements to the stellar dynamical black hole mass exceeding the gas dynamical determination by a factor of five. Of the three cases in which the black hole masses disagree, the stellar dynamical measurement is always larger than the black hole mass derived with gas dynamical modeling. With such a limited sample, clearly more cross-checks are necessary before conclusions can be made regarding the consistency of the gas and stellar dynamical techniques, the subsequent effects on the $M_{\text{BH}} - \text{host galaxy}$ relationship, and the magnitude and distribution of the cosmic scatter in the correlations. Targeting galaxies with dust lanes could be particularly useful, as

well-ordered, symmetric dust lanes suggest the presence of a regularly rotating gas disk (Ho et al. 2002) and can also be used to constrain galaxy inclinations.

We would like to thank Shelley Wright for her assistance with the OSIRIS observations, and Ronald Läsker and his collaborators for sharing their CFHT WIRCam image of NGC 3998 prior to publication. We also thank the anonymous referee for a thoughtful and quick response, which helped improve the manuscript. Research by A. J. B. and J. L. W. has been supported by NSF grants AST-0548198 and AST-1108835. J. L. W. has also been supported by an NSF Astronomy and Astrophysics Postdoctoral Fellowship under Award No. 1102845. Some of the data presented herein were obtained at the W. M. Keck Observatory, which is operated as a scientific partnership among the California Institute of Technology, the University of California and the National Aeronautics and Space Administration. The Observatory was made possible by the generous financial support of the W. M. Keck Foundation. We wish to recognize and acknowledge the very significant cultural role and reverence that the summit of Mauna Kea has always had within the indigenous Hawaiian community. We are most fortunate to have the opportunity to conduct observations from this mountain. All of the stellar dynamical models presented in this work were run on the THEO cluster at the Rechenzentrum Garching (RZG) of the Max Planck Society. Some of the data presented in this paper were obtained from the Multimission Archive at the Space Telescope Science Institute (MAST). STScI is operated by the Association of Universities for Research in Astronomy, Inc., under NASA contract NAS5-26555. This research has made use of the NASA/IPAC Extragalactic Database (NED), which is operated by the Jet Propulsion Laboratory, California Institute of Technology, under contract with NASA. We acknowledge the usage of the HyperLeda database (<http://leda.univ-lyon1.fr>).

REFERENCES

- Bacon, R., et al. 2001, *MNRAS*, 326, 23
- Baggett, W. E., Baggett, S. M., Anderson, K. S. J. 1998, *AJ*, 116, 1626
- Barth, A. J., Sarzi, M., Rix, H.-W., Ho, L. C., Filippenko, A. V., & Sargent, W. L. W. 2001, *ApJ*, 555, 685
- Beifiori, A., Sarzi, M., Corsini, E. M., Dalla Bontà, E., Pizzella, A., Coccato, & L., Bertola, F. 2009, *ApJ*, 692, 856
- Bender, R., Saglia, R. P., & Gerhard, O. E. 1994, *MNRAS*, 269, 785
- Binney, J., & Tremaine, S. 1987, *Galactic Dynamics*, ed. Binney, J. & Tremaine, S.
- Bostroem, K., & Proffitt, C. 2011, *STIS Data Handbook*, Version 6.0 (Baltimore:STScI)
- Bower, G. A., Wilson, A. S., Heckman, T. M., Magorrian, J., Gebhardt, K., Richstone, D. O., Peterson, B. M., & Green, R. F. 2000, *BAAS*, 32, 1566
- Bower, G. A., et al. 2001, *ApJ*, 550, 75
- Cappellari, M. 2002a, *MNRAS*, 333, 400
- Cappellari, M., Verolme, E. K., van der Marel, R. P., Kleijn, G. A. V., Illingworth, G. D., Franx, M., Carollo, C. M., & de Zeeuw, P. T. 2002b, *ApJ*, 578, 787
- Cappellari, M., & Copin, Y. 2003, *MNRAS*, 342, 345
- Cappellari, M., & Emsellem, E. 2004, *PASP*, 116, 138
- Cappellari, M., et al. 2006, *MNRAS*, 366, 1126
- Cappellari, M., Neumayer, N., Reunanen, J., van der Werf, P. P., de Zeeuw, P. T., & Rix, H.-W. 2009, *MNRAS*, 394, 660
- Cappellari, M., et al. 2012, arXiv:1202.3308
- Cretton, N., de Zeeuw, P. T., van der Marel, R. P., & Rix, H.-W. 1999, *ApJS*, 124, 383
- Dalla Bontà, E., Ferrarese, L., Corsini, E. M., Miralda-Escudé, J., Coccato, L., Sarzi, M., Pizzella, A., & Beifiori, A. 2009, *ApJ*, 690, 537
- Davies, R. L., Tacconi, L., Genzel, R., Ott, T., & Rabien, S. 2004, *Proc. SPIE*, 5490, 473
- Davies, R. I., et al. 2006, *ApJ*, 646, 754
- Davies, R. I. 2007, *MNRAS*, 375, 1099
- de Francesco, G., Capetti, A., & Marconi, A. 2006, *A&A*, 460, 439
- de Vaucouleurs, G., de Vaucouleurs, A., Corwin, H. G., Buta, R. J., Paturel, G., & Fouque, P. 1991, *Third Reference Catalogue of Bright Galaxies* (New York: Springer-Verlag)
- Di Matteo, T., Springel, V., & Hernquist, L. 2005, *Nature*, 433, 604
- Dolphin, A. E. 2000, *PASP*, 112, 1397
- Dressler, A. 1989, in *IAU Symp. 134, Active Galactic Nuclei*, ed. D. E. Osterbrock & J. S. Miller (Dordrecht: Kluwer), 217
- Fabbiano, G., Fassnacht, C., & Trinchieri, G. 1994, *ApJ*, 434, 67
- Ferrarese, L., & Merritt, D. 2000, *ApJL*, 539, L9
- Fisher, D., Franx, M., & Illingworth, G. 1996, *ApJ*, 459, 110
- Forestell, A. D., & Gebhardt, K. 2010, *ApJ*, 716, 370
- Gebhardt, K., et al. 2000a, *AJ*, 119, 1157
- Gebhardt, K., et al. 2000b, *ApJL*, 539, L13
- Gebhardt, K., et al. 2003, *ApJ*, 583, 92
- Gebhardt, K., & Thomas, J. 2009, *ApJ*, 700, 1690
- Gebhardt, K., Adams, J., Richstone, D., Lauer, T. R., Faber, S. M., Gültekin, K., Murphy, J., & Tremaine, S. 2011, *ApJ*, 729, 119
- González Delgado, R. M., Pérez, E., Cid Fernandes, R., & Schmitt, H. 2008, *AJ*, 135, 747
- Graham, A. W., Onken, C. A., Athanassoula, E., & Combes, F. 2011, *MNRAS*, 412, 2211
- Gültekin, K., et al. 2009a, *ApJ*, 695, 1577
- Gültekin, K., et al. 2009b, *ApJ*, 698, 198
- Häring-Neumayer, N., Cappellari, M., Rix, H.-W., Hartung, M., Prieto, M. A., Meisenheimer, K., & Lenzen, R. 2006, *ApJ*, 643, 26
- Harms, R. J., et al. 1994, *ApJL*, 435, L35
- Hicks, E. K. S., & Malkan, M. A. 2008, *ApJS*, 174, 31
- Ho, L. C., Filippenko, A. V., & Sargent, W. L. W. 1993, *ApJ*, 417, 63
- Ho, L. C., Filippenko, A. V., & Sargent, W. L. W. 1997, *ApJS*, 112, 315
- Ho, L. C., Sarzi, M., Rix, H.-W., Shields, J. C., Rudnick, G., Filippenko, A. V., & Barth, A. J. 2002, *PASP*, 114, 137
- Houghton, R. C. W., Magorrian, J., Sarzi, M., Thatte, N., Davies, R. L., & Krajnović, D. 2006, *MNRAS*, 367, 2
- Hummel, E., van der Hulst, J. M., & Dickey, J. M. 1984, *A&A*, 134, 207
- Jahnke, K., & Macciò, A. V. 2011, *ApJ*, 734, 92
- Jardel, J. R., et al. 2011, *ApJ*, 739, 21
- Kormendy, J., & Richstone, D. 1995, *ARA&A*, 33, 581
- Krajnović, D., Cappellari, M., Emsellem, E., McDermid, R. M., & de Zeeuw, P. T. 2005, *MNRAS*, 357, 1113
- Krajnović, D., Sharp, R., & Thatte, N. 2007, *MNRAS*, 374, 385
- Krajnović, D., McDermid, R. M., Cappellari, M., & Davies, R. L. 2009, *MNRAS*, 399, 1839
- Krist, J., & Hook, R. 2004, *The Tiny Tim User's Guide* (Baltimore:STScI)
- Larkin, J., et al. 2006, *Proc. SPIE*, 6269, 42
- Macchetto, F., Marconi, A., Axon, D. J., Capetti, A., Sparks, W., & Crane, P. 1997, *ApJ*, 489, 579
- Magorrian, J., et al. 1998, *AJ*, 115, 2285
- Maoz, D., Nagar, N. M., Falcke, H., & Wilson, A. S. 2005, *ApJ*, 625, 699
- Marconi, A., Capetti, A., Axon, D. J., Koekemoer, A., Macchetto, D., & Schreier, E. J. 2001, *ApJ*, 549, 915
- Marconi, A., & Hunt, L. K. 2003, *ApJL*, 589, L21
- Marconi, A., Pastorini, G., Pacini, F., Axon, D. J., Capetti, A., Macchetto, D., Koekemoer, A. M., & Schreier, E. J. 2006, *A&A*, 448, 921
- McConnell, N. J., Ma, C.-P., Graham, J. R., Gebhardt, K., Lauer, T. R., Wright, S. A., & Richstone, D. O. 2011a, *ApJ*, 728, 100
- McConnell, N. J., Ma, C.-P., Gebhardt, K., Wright, S. A., Murphy, J. D., Lauer, T. R., Graham, J. R., & Richstone, D. O. 2011b, *Nature*, 480, 215
- Mei, S., et al. 2007, *ApJ*, 655, 144
- Murphy, J. D., Gebhardt, K., & Adams, J. J. 2011, *ApJ*, 729, 129
- Navarro, J. F., Frenk, C. S., & White, S. D. M. 1996, *ApJ*, 462, 563
- Neumayer, N., Cappellari, M., Reunanen, J., Rix, H.-W., van der Werf, P. P., de Zeeuw, P. T., & Davies, R. I. 2007, *ApJ*, 671, 1329
- Neumayer, N., & Walcher, C. J. 2012, arXiv:1201.4950
- Nowak, N., Thomas, J., Erwin, P., Saglia, R. P., Bender, R., & Davies, R. I. 2010, *MNRAS*, 403, 646
- Oke, J. B., et al. 1995, *PASP*, 107, 375
- Onken, C. A., et al. 2007, *ApJ*, 670, 105
- Paturel, G., Petit, C., Prugniel, P., Theureau, G., Rousseau, J., Brouty, M., Dubois, P., & Cambrésy, L. 2003, *A&A*, 412, 45
- Pellegrini, S., Cappi, M., Bassani, L., della Ceca, R., & Palumbo, G. G. C. 2000, *A&A*, 360, 878
- Peng, C. Y. 2007, *ApJ*, 671, 1098
- Puget, P., et al. 2004, *SPIE*, 5492, 978
- Richstone, D., et al. 1998, *Nature*, 395, 14
- Rix, H.-W., de Zeeuw, P. T., Cretton, N., van der Marel, R. P., & Carollo, C. M. 1997, *ApJ*, 488, 702
- Roberts, T. P., & Warwick, R. S. 2000, *MNRAS*, 315, 98
- Rusli, S. P., Thomas, J., Erwin, P., Saglia, R. P., Nowak, N., & Bender, R. 2011, *MNRAS*, 410, 1223
- Sánchez-Portal, M., Díaz, Á. I., Terlevich, E., & Terlevich, R. 2004, *MNRAS*, 350, 1087
- Sani, E., Marconi, A., Hunt, L. K., & Risaliti, G. 2011, *MNRAS*, 413, 1479
- Schlegel, D. J., Finkbeiner, D. P., & Davis, M. 1998, *ApJ*, 500, 525
- Schulze, A., & Gebhardt, K. 2011, *ApJ*, 729, 21
- Schwarzschild, M. 1979, *ApJ*, 232, 236
- Shapiro, K. L., Cappellari, M., de Zeeuw, T., McDermid, R. M., Gebhardt, K., van den Bosch, R. C. E., & Statler, T. S. 2006, *MNRAS*, 370, 559
- Shen, J., & Gebhardt, K. 2010, *ApJ*, 711, 484
- Silge, J. D., Gebhardt, K., Bergmann, M., & Richstone, D. 2005, *AJ*, 130, 406
- Silk, J., & Rees, M. J. 1998, *A&A*, 331, L1
- Statler, T. 1995, *AJ*, 109, 1371
- Thomas, J., Saglia, R. P., Bender, R., Thomas, D., Gebhardt, K., Magorrian, J., Corsini, E. M., & Wegner, G. 2005, *MNRAS*, 360, 1355
- Thomas, J., Saglia, R. P., Bender, R., Thomas, D., Gebhardt, K., Magorrian, J., Corsini, E. M., & Wegner, G. 2007, *MNRAS*, 382, 657
- Thomas, J., Saglia, R. P., Bender, R., Thomas, D., Gebhardt, K., Magorrian, J., Corsini, E. M., & Wegner, G. 2009, *ApJ*, 691, 770
- Tonry, J. L., et al. 2001, *ApJ*, 546, 681
- Tremaine, S., et al. 2002, *ApJ*, 574, 740
- Valluri, M., Merritt, D., & Emsellem, E. 2004, *ApJ*, 602, 66
- Valluri, M., Ferrarese, L., Merritt, D., & Joseph, C. L. 2005, *ApJ*, 628, 137
- van Dam, M. A., et al. 2006, *PASP*, 118, 310
- van Dokkum, P. G. 2001, *PASP*, 113, 1420
- van Dokkum, P. G., & Conroy, C. 2010, *Nature*, 468, 940
- van den Bosch, R. C. E., van de Ven, G., Verolme, E. K., Cappellari, M., & de Zeeuw, P. T. 2008, *MNRAS*, 385, 647
- van den Bosch, R. C. E., & van de Ven, G. 2009, *MNRAS*, 398, 1117
- van den Bosch, R. C. E., & de Zeeuw, P. T. 2010, *MNRAS*, 401, 1770
- van der Marel, R. P., & Franx, M. 1993, *ApJ*, 407, 525
- van der Marel, R. P., Cretton, N., de Zeeuw, P. T., & Rix, H.-W. 1998a, *ApJ*, 493, 613
- van der Marel, R. P., & van den Bosch, F. C. 1998b, *AJ*, 116, 2220
- Verdoes Kleijn, G. A., van der Marel, R. P., Carollo, C. M., & de Zeeuw, P. T. 2000, *AJ*, 120, 221
- Verdoes Kleijn, G. A., van der Marel, R. P., de Zeeuw, P. T., Noel-Storr, J., & Baum, S. A. 2002, *AJ*, 124, 2524

Verolme, E. K., & de Zeeuw, P. T. 2002a, MNRAS, 331, 959
Verolme, E. K., et al. 2002b, MNRAS, 335, 517
Walsh, J. L., Barth, A. J., & Sarzi, M. 2010, ApJ, 721, 762

Weijmans, A.-M., et al. 2009, MNRAS, 398, 561
Wizinowich, P. L., et al. 2006, PASP, 118, 297